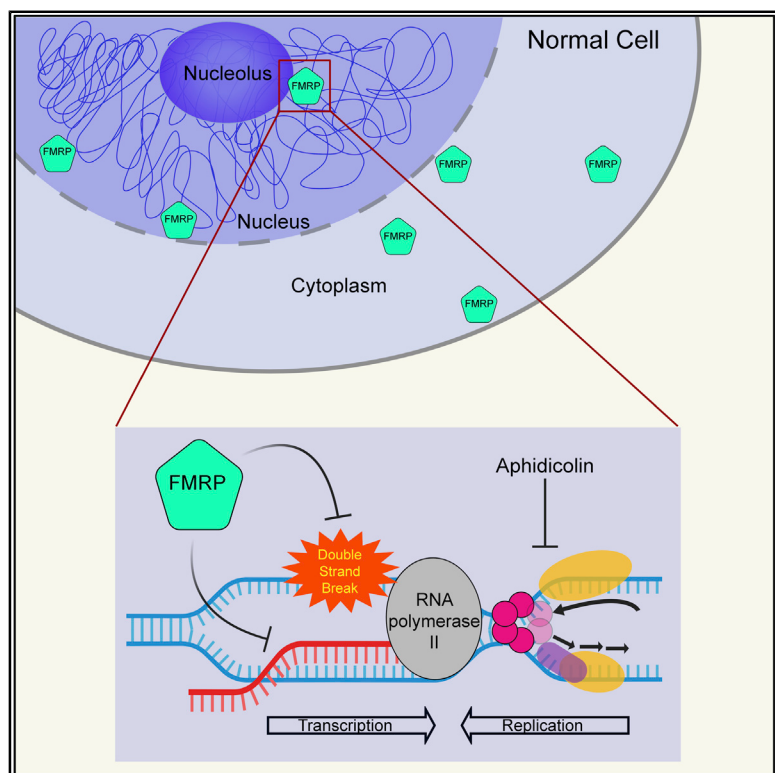


## Replication Stress Induces Global Chromosome Breakage in the Fragile X Genome

### Graphical Abstract



### Authors

Arijita Chakraborty, Piroon Jenjaroenpun, Jing Li, ..., Chun-long Chen, Vladimir A. Kuznetsov, Wenyi Feng

### Correspondence

fengw@upstate.edu

### In Brief

Chakraborty et al. report a genome-wide increase of DNA double-strand breaks in fragile X syndrome patient cells and suggest that FMRP functions in the R-loop pathway to prevent genome instability induced by DNA replication-transcription conflicts.

### Highlights

- Fragile X cells have increased DNA damage with or without DNA replication stress
- Break-seq identifies genome-wide DNA double-strand breaks in fragile X cells
- Fragile X cells have elevated R-loop formation under DNA replication stress
- FMRP, but not a disease-causing FMRP-I304N mutant, reduces R-loop-induced DSBs



## Article

## Replication Stress Induces Global Chromosome Breakage in the Fragile X Genome

Arijita Chakraborty,<sup>1</sup> Piroon Jenjaroenpun,<sup>2,8</sup> Jing Li,<sup>1</sup> Sami El Hilali,<sup>3,4</sup> Andrew McCulley,<sup>1</sup> Brian Haarer,<sup>1</sup> Elizabeth A. Hoffman,<sup>1,9</sup> Aimee Belak,<sup>5,10</sup> Audrey Thorland,<sup>5,11</sup> Heidi Hehnly,<sup>5</sup> Carl Schildkraut,<sup>6</sup> Chun-long Chen,<sup>3,4</sup> Vladimir A. Kuznetsov,<sup>2,7</sup> and Wenyi Feng<sup>1,12,\*</sup>

<sup>1</sup>Department of Biochemistry and Molecular Biology, SUNY Upstate Medical University, 750 East Adams Street, Syracuse, NY 13210, USA

<sup>2</sup>Bioinformatics Institute, Agency for Science Technology and Research (A\*STAR), 30 Biopolis Street, #07-01 Matrix, Singapore 138671, Singapore

<sup>3</sup>Institut Curie, PSL Research University, CNRS, UMR3244, 75005 Paris, France

<sup>4</sup>Sorbonne Université, 75005 Paris, France

<sup>5</sup>Department of Biology, Syracuse University, Syracuse, NY 13210, USA

<sup>6</sup>Department of Cell Biology, Albert Einstein College of Medicine, New York, NY 10461, USA

<sup>7</sup>Department of Urology, SUNY Upstate Medical University, 750 East Adams Street, Syracuse, NY 13210, USA

<sup>8</sup>Present address: Department of Biomedical Informatics, University of Arkansas for Medical Sciences, Little Rock, AR 72205, USA

<sup>9</sup>Present address: AAAS Science & Technology Policy Fellowship hosted at National Institute of Standards and Technology (NIST), Gaithersburg, MD, USA

<sup>10</sup>Present address: University of Maryland School of Medicine, 655 W. Baltimore Street, Baltimore, MD 21201, USA

<sup>11</sup>Present address: Department of Clinical Laboratory Sciences, SUNY Upstate Medical University, 750 East Adams Street, Syracuse, NY 13210, USA

<sup>12</sup>Lead Contact

\*Correspondence: [fengw@upstate.edu](mailto:fengw@upstate.edu)

<https://doi.org/10.1016/j.celrep.2020.108179>

## SUMMARY

Fragile X syndrome (FXS) is a neurodevelopmental disorder caused by mutations in the *FMR1* gene and deficiency of a functional FMRP protein. FMRP is known as a translation repressor whose nuclear function is not understood. We investigated the global impact on genome stability due to FMRP loss. Using Break-seq, we map spontaneous and replication stress-induced DNA double-strand breaks (DSBs) in an FXS patient-derived cell line. We report that the genomes of FXS cells are inherently unstable and accumulate twice as many DSBs as those from an unaffected control. We demonstrate that replication stress-induced DSBs in FXS cells colocalize with R-loop forming sequences. Exogenously expressed FMRP in FXS fibroblasts ameliorates DSB formation. FMRP, not the I304N mutant, abates R-loop-induced DSBs during programmed replication-transcription conflict. These results suggest that FMRP is a genome maintenance protein that prevents R-loop accumulation. Our study provides insights into the etiological basis for FXS.

## INTRODUCTION

Fragile X syndrome (FXS) is responsible for the most common form of inherited intellectual disability (ID) and autism (Santoro et al., 2012). In most patients, FXS is caused by (CGG)<sub>n</sub> trinucleotide repeat expansion exceeding 200 copies in the 5' untranslated region of *FMR1* located on Xq27.3 (Fu et al., 1991; Verkerk et al., 1991). This repeat expansion mutation then leads to heterochromatin formation and epigenetic silencing (Coffee et al., 2002; Pieretti et al., 1991). Studies have shown that both full mutation-size (>200 copies) and carrier-size (50–200 copies) (CGG)<sub>n</sub> repeats stall replication forks (Gerhardt et al., 2014; Voineagu et al., 2009) and lead to double-strand break (DSB) and chromosome fragile site formation (Krawczun et al., 1985), hence the name of the disease. FXS can also manifest as a result of mutations in the FMRP coding sequence despite a normal range of (CGG)<sub>n</sub> repeats, highlighting the functional importance of

FMRP to the etiological basis for FXS (Ciaccio et al., 2017). A recent study showed that (CGG)<sub>n</sub> repeat expansion below the gene silencing threshold can induce break-induced repair pathway, resulting in mutations in the distal region downstream of the promoter (Kononenko et al., 2018). This observation provided an elegant mechanism linking repeat expansion and exonic mutations in *FMR1*.

FMRP is estimated to bind ~4% of the mRNAs in the brain and regulate their translation (Ashley et al., 1993). It is clear that FMRP has multifaceted cellular functions. The best-understood one is translation repression of the metabotropic glutamate receptor (mGluR)-mediated long-term depression (LTD) (Bear et al., 2004). FMRP deficiency permits an increased level of protein synthesis at postsynaptic dendrites and prolonged LTD, thus causing many of the symptoms of FXS (Bear et al., 2004; Darnell et al., 2011; Nakamoto et al., 2007; Niere et al., 2012). Genome-wide studies have identified >6,000 FMRP-interacting mRNAs,



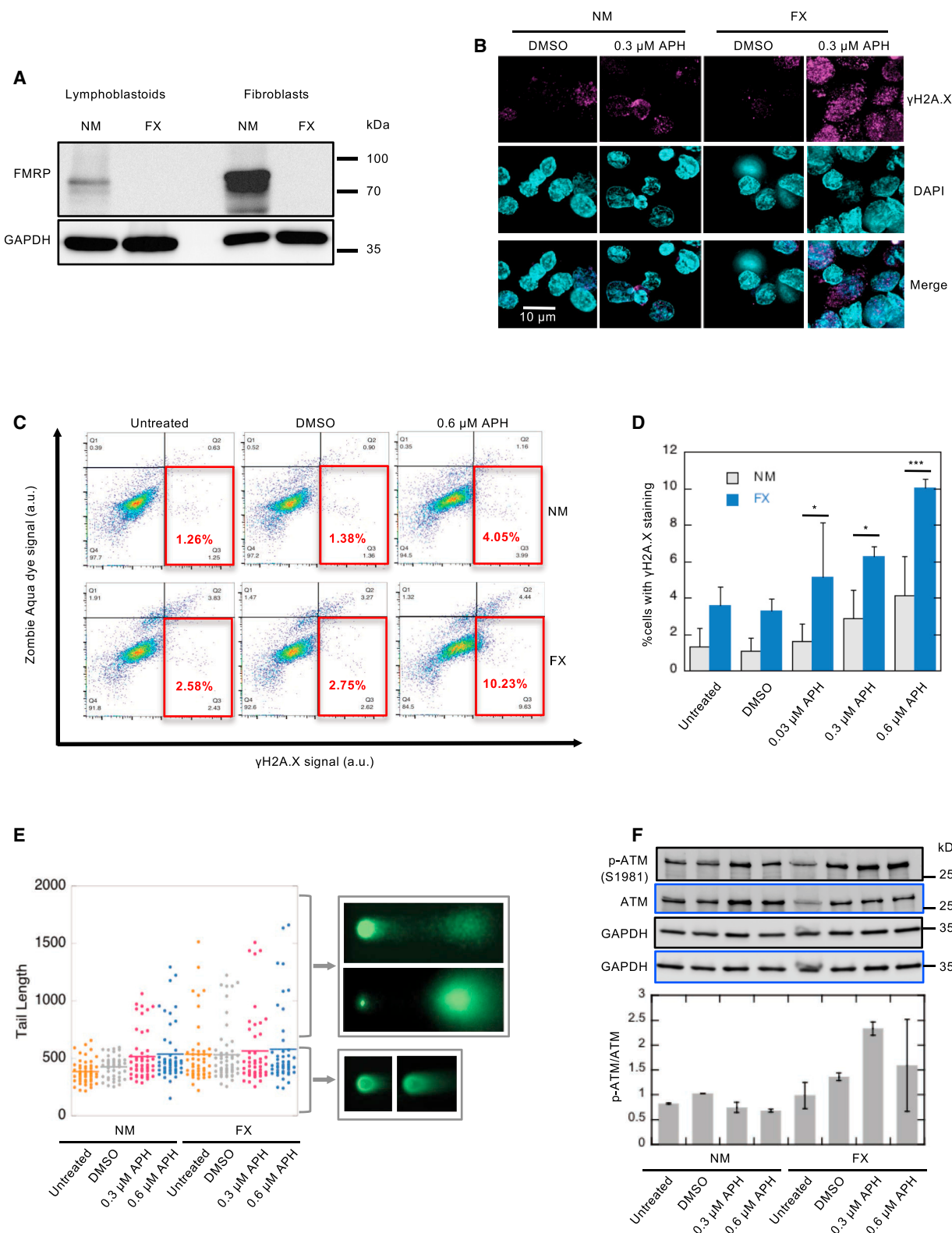


**Figure 1. Fragile X (FX) Cells Show Elevated DNA Damage under Replication Stress and an Intact DDR**

(A) Western blots confirming the absence of FMRP expression in FX cell lines.

(B) Increased γH2A.X foci formation in FX lymphoblastoid cells in APH. Scale bar, 10 μm. See also Figure S2.

(legend continued on next page)

many of which are involved in synaptic signaling and function (Ashley et al., 1993; Brown et al., 2001; Darnell et al., 2011). Only a small percentage of these putative FMRP targets have been validated by independent methods (Sethna et al., 2014) and mGluR antagonist drugs have yet to show efficacy in human patients, despite preclinical success in animal models (Erickson et al., 2017). Consistent with its role as a translation repressor, FMRP is predominantly located in the cytoplasm and associates with the polysomes (Darnell et al., 2011; Khandjian et al., 2004). However, FMRP also has nuclear presence (Feng et al., 1997) and it has been found to interact with its mRNA substrates in the nucleus (Kim et al., 2009). Thus, FMRP likely plays a role in the nucleocytoplasmic shuttling of the mRNA cargoes, but its additional nuclear function(s) remains elusive.

A recent study reported that FMRP is enriched in the nucleus during replication stress, suggesting a chromatin-related function of FMRP (Alpatov et al., 2014). The authors showed that *fmr1*<sup>-/-</sup> mouse embryonic fibroblasts produced decreased γH2A.X staining, compared to control cells, during replication stress by aphidicolin (APH, a DNA polymerase inhibitor). This observation led to the conclusion that *fmr1*<sup>-/-</sup> cells are deficient in the DNA damage response (DDR) (Alpatov et al., 2014). It was also reported that *Drosophila* dFMRP1-deficient cells showed decreased γH2A.X foci formation when treated with hydroxyurea, an inhibitor of ribonucleotide reductase that results in reduced deoxyribonucleotide pools (Zhang et al., 2014). However, dFMRP1-deficient cells were also shown to be hypersensitive to genotoxic chemicals, including hydroxyurea, increased chromosome breaks, and increased γH2Av foci formation upon irradiation (Liu et al., 2012). Therefore, it remains unclear whether cells lacking FMRP sustain increased or decreased levels of DNA damage, despite a consensus view that FMRP is involved in DDR.

In this study, we asked whether the lack of FMRP leads to genome instability. We used lymphoblastoids and fibroblasts derived from FXS patients with full mutations of *FMR1* and unaffected controls and subjected them to a multitude of queries. We consistently observed increased levels of DNA damage, manifested as increased γH2A.X staining and long comet tails in a single-molecule DNA breakage assay, occurring both spontaneously and inducible by APH, in FXS cells. We further demonstrated that exogenously expressed FMRP in FXS cells reduced the APH-induced DSB formation. More important, we mapped genome-wide DNA DSBs in FXS lymphoblastoid cells using Break-seq (Hoffman et al., 2015). We demonstrated that Break-seq, when adapted to the mammalian cell system, maintains high sensitivity and specificity, owing to the innovative approach of encapsulating cells in agarose plugs to minimize *in vitro* production of DSBs. We also demonstrated that the patient-derived lymphoblastoids contained molecular signatures

for FXS. Lymphoblastoid cells have been previously used to reveal the genetic basis of a range of neurological disorders, including FXS (Kollipara et al., 2017; Nishimura et al., 2007; Pan-sarasa et al., 2018). Here, we show that the FXS cells exhibited a >2-fold increase in the number of DSBs compared to controls. We further demonstrated that replication stress-induced DSBs were enriched at R-loop forming sequences (RLFs), where the RNA transcript hybridizes to homologous DNA on the chromosome, yielding a RNA:DNA hybrid and a displaced DNA single strand. Despite their many roles in normal cellular functions, R-loops can initiate conflicts between transcription and replication by creating a barrier to replication fork progression, causing DSBs (García-Rubio et al., 2018; Hamperl et al., 2017). Thus, we hypothesized that FXS cells are susceptible to R-loop formation during replication stress. We present evidence that FMRP, when provided exogenously, can reduce DSBs within genes prone to R-loop formation during transcription, particularly during programmed replication-transcription conflicts in a model system.

## RESULTS

### Fragile X Cells Sustain Elevated DNA Damage under Replication Stress

We chose cells derived from individuals diagnosed with FXS (henceforth “FX”) and unaffected normal individuals (henceforth “NM”) from two tissue origins for this study. Lymphoblastoid cells derived from an individual with a full mutation of *FMR1* (GM03200) and an unaffected individual with a normal *FMR1* (GM06990) were used for the majority of the study, unless otherwise noted. Select experiments also used fibroblasts from an individual with a full mutation of *FMR1* (GM05848), in comparison to those derived from a sex- and age-matched control (GM00357). We confirmed the lack of FMRP expression by western blot in the FX cell lines (Figure 1A) and CGG repeat expansions, ~570 repeats in GM03200 and ~730 in GM05848, by Southern blot (Figures S1A and S1B).

We then analyzed genome instability in the lymphoblastoid cell lines by partially inhibiting replication with aphidicolin (APH, a DNA polymerase inhibitor) and causing a 10%–20% increase in cells in S phase (Figure S1C). Both cell lines showed a dose-dependent increase in DSBs upon APH treatment, evidenced by increased immunostaining of γH2A.X (a marker for DNA DSBs) (Figures 1B and S2A). This observation was confirmed in FX fibroblasts (Figures S2B and S2C). The quantification of cells with γH2A.X expression using flow cytometry further corroborated that FX cells showed a >2-fold increase in the γH2A.X level compared to controls, with and without replication stress (Figures 1C and 1D). These results suggested that the loss of FMRP caused heightened levels of DSB formation both spontaneously and upon APH-induced replication stress. We next

(C and D) Analysis of γH2A.X signal under APH induction by flow cytometry. The solid red boxes indicate the gated live cells, with γH2A.X signals greater than baseline. Two-way ANOVA followed by Sidak's multiple testing was performed. Error bars indicate standard deviation. \* $p < 0.05$  and \*\*\* $p < 0.001$ .

(E) DSB formation measured by neutral Comet assay. Three independent experiments were performed ( $n > 50$  in each) and all trended similarly. The tail lengths from one representative experiment are shown in the boxplot. Representative images of comets with short or long Comet tail lengths are shown.

(F) Expression of phospho-ataxia telangiectasia mutated (p-ATM) in NM and FX lymphoblastoid cells indicates intact DDR in FX cells. Western blots probed with anti-p-ATM and total ATM are shown in black- and blue-bordered panels, respectively. Both blots were controlled for loading using anti-glyceraldehyde 3-phosphate dehydrogenase (GAPDH). The ratios of p-ATM:total ATM are shown below the blots. The error bars indicate standard errors of the mean.

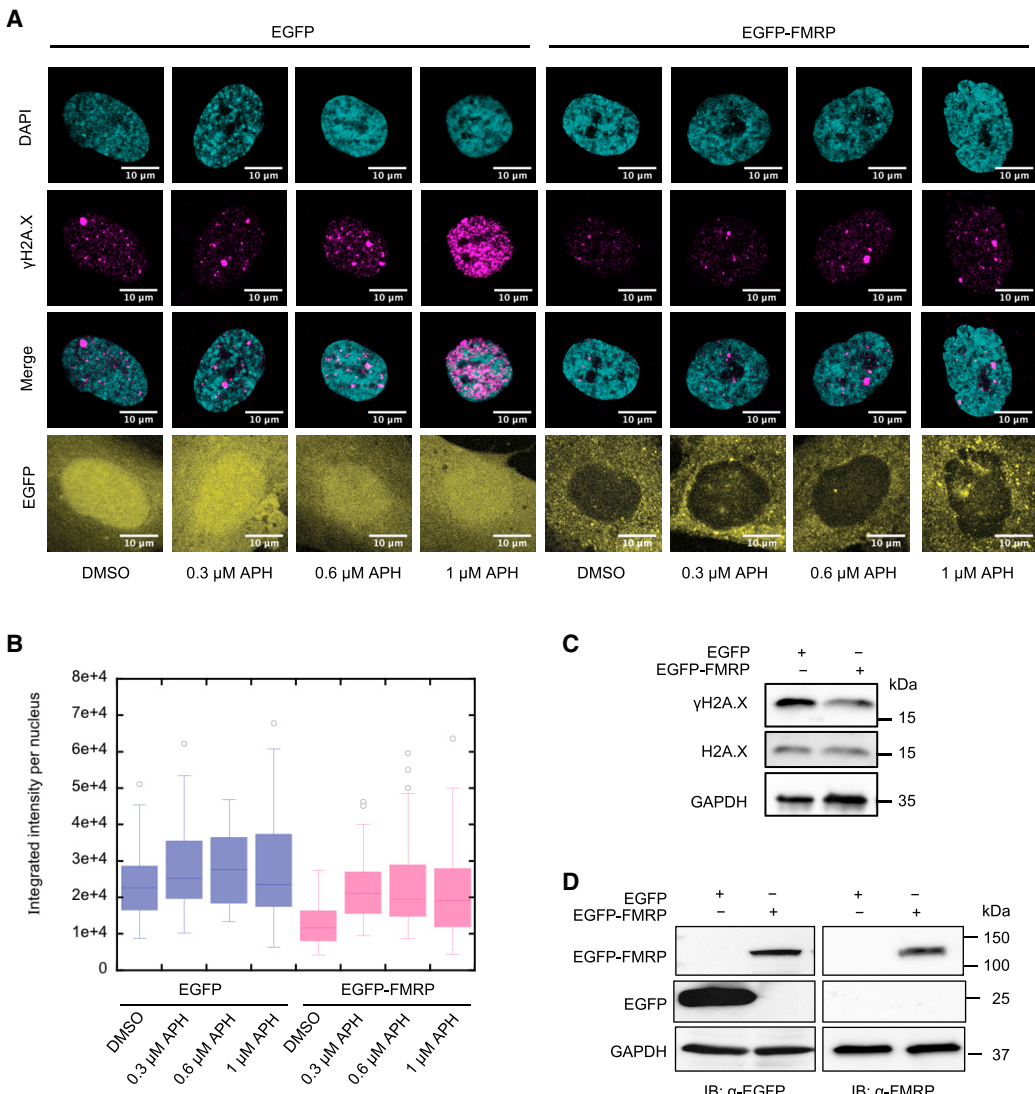


**Figure 2. FMRP Expression Ameliorates APH-Induced DSB Formation in FX Cells**

(A)  $\gamma$ H2A.X immunofluorescence in FX fibroblast cells (GM05848) carrying pMSCVpuro-EGFP or pMSCVpuro-EGFP-FMRP. Scale bar, 10  $\mu$ m.  
(B) Quantitation of the  $\gamma$ H2A.X immunofluorescence signals in (A) by boxplot.  
(C) EGFP and EGFP-FMRP fusion protein expression in the respective cells in (A).

performed a neutral Comet assay to investigate DSB formation at a single-cell level. The results were consistent with the  $\gamma$ H2A.X staining experiments—FX cells showed a higher level of DSBs than their control counterparts (Figure S3A). In addition, the comet tail length distribution showed that compared to control cells, FX cells had longer comet tails, often severed from the comet heads, suggesting more severe DNA damage (Figure 1E); this is consistent with the observed increase in  $\gamma$ H2A.X staining. To determine whether FX cells also suffered from a defective DNA damage response (DDR), we examined the phosphorylation of multiple components of the DDR pathway by western blots. FX cells showed higher levels of phospho(p)-ataxia telangiectasia mutated (ATM), p-replication protein A (RPA2), and  $\gamma$ H2A.X than control cells, suggesting a more robust activation

of the DDR in FX cells (Figures 1F, S3B, and S3C). The levels of p-ataxia telangiectasia and Rad3 related (ATR) and p-checkpoint kinase 1 (CHEK1) were similar in both cells. Next, we asked whether the increased susceptibility to DNA damage by the FX genome was due to the absence of FMRP.

#### Ectopic Expression of FMRP Reduces APH-Induced DNA Damage in the FXS Patient-Derived Fibroblasts

We transduced the FX fibroblasts (GM05448) with a plasmid carrying EGFP-FMRP fusion, or a plasmid carrying EGFP alone as a negative control. We then subjected the resulting cell lines to APH treatment at increasing concentrations. Cells expressing EGFP-FMRP showed reduced  $\gamma$ H2A.X signals compared to control cells expressing EGFP alone (Figure 2A). The

quantification of results recapitulated the dose-dependent increase of  $\gamma$ H2A.X signals by APH treatment in cells expressing EGFP-FMRP (1-way ANOVA,  $p = 0.00018$ ), albeit not in control cells (One-way ANOVA,  $p = 0.34$ ) (Figure 2B). More important, cells expressing EGFP-FMRP showed systematically reduced DNA damage by APH compared to control cells (Two-way ANOVA,  $p = 5.49E-6$ ). This result was confirmed by the reduced expression of  $\gamma$ H2A.X in EGFP-FMRP<sup>+</sup> cells (Figure 2C). We also confirmed that EGFP-FMRP expression was only detected in the cells carrying the EGFP-FMRP plasmid both by anti-GFP and by anti-FMRP in western blots (Figure 2D). Therefore, we concluded that the replication stress-induced DNA damage in FX cells was due to the absence of FMRP. This prompted us to further investigate the locations of DNA DSBs in FX cells.

### Genome-wide DSB Mapping by Break-Seq

Here, we adapted Break-seq, a powerful technology we first developed in yeast (Hoffman et al., 2015), to the mammalian system and mapped genome-wide chromosome breaks in untreated cells and cells treated with APH or with equal volume of the vehicle, dimethyl sulfoxide (DMSO) (Figure 3A). Each strain/treatment combination was represented by at least two independent experiments. As a proof-of-principle, we mapped DSBs produced by *in vitro* *PacI* digestion of DNA from FX cells treated with DMSO or 0.03  $\mu$ M APH (Figure 3B). More than 96% of DSBs mapped in these 2 samples corresponded to a known *PacI* site ( $p < 2.2E-16$  in random permutation tests with 1,000 iterations, see Method Details), with  $\geq 83\%$  concordance between them (Figure 3B). Of the 151,583 *PacI* sites in the human hg19 genome, 84,458 (56%) and 87,727 (58%) were mapped in the DMSO and APH samples, respectively. These results provided a benchmark for Break-seq, with  $>97\%$  specificity and  $>56\%$  sensitivity (the in-gel digestion efficiency of *PacI* was estimated at  $\sim 70\%$ , suggesting a true Break-seq sensitivity of  $\sim 80\%$ ). Break-seq library qualities were assessed by read classification and hierarchical clustering (Figures S4A–S4C). At the present sequencing depth, recurrent DSBs were identified, although Break-seq libraries were not saturated (Figure S4D). For each strain/treatment combination, for instance “FX\_0.03  $\mu$ M APH,” “consensus DSBs” from at least two replicate experiments, regardless of the total number of replicates, were derived (Figure 3C). The DSBs from 0.03 and 0.3  $\mu$ M APH-treated samples were further pooled into a composite dataset of “FX\_APH,” for each cell line, followed by comparison with the DMSO-treated control to identify DSBs shared by DMSO and APH treatment as well as those specific to each treatment (Figure 3C). DSB hotspots were distributed throughout the genome and with apparent enrichment in the pericentric regions (Figure 3D).

In all of the experiments, FX cells produced 2- to 2.5-fold more DSBs than NM cells with or without drugs (Figure 4A; Table S1), consistent with high levels of  $\gamma$ H2A.X signal observed in FX cells. X chromosome showed the highest density of DSBs in APH-induced FX cells, at approximately eight DSBs per megabase of DNA (Figure 4B). Overall, 83%, 16%, and 62% of DSBs in the untreated, DMSO-treated, and APH-treated NM cells, respectively, were found in the corresponding treatments of FX cells (Figure 4C). This result suggested that spontaneous DSBs were largely concordant between the two cell lines. We exam-

ined the relative dissimilarity between DSBs in DMSO-treated NM and FX cells. We found that untreated and DMSO-treated FX cells only shared 8% common DSBs, in contrast to 78% concordance between untreated and DMSO-treated NM cells. These observations suggested that DMSO treatment caused FX cells to “reprogram” DSB formation compared to NM cells. Lastly, in both cell lines the dual treatment of DMSO and APH enhanced existent DSBs (from DMSO treatment alone), with a greater extent of new DSB induction in the FX cells: there was 82% and 67% concordance between DMSO-treated and dual APH-treated samples for NM and FX cells, respectively. Here, we concluded that drug treatment in FX cells elicited a different response than in NM cells. We proceeded to investigate the mechanism of DSB induction.

### DSBs and Replication Timing

APH-induced DSBs are definable as a genomic feature called common fragile sites (CFSs) (Glover et al., 1984). We systematically compared the APH-induced DSBs mapped in our study to CFSs reported in the literature that are also present in lymphocytes, the same cell type as was used in our study, including 52 CFSs from Savelyeva and Brueckner (2014) and 24 CFSs from Le Tallec et al. (2013). We also compared our DSBs to a list of DSBs mapped by a genome-wide technique named BLESS in APH-treated HeLa cells (“APH.breakome”) (Crosetto et al., 2013). We did not find significant ( $p < 0.001$ ) correlation between DSBs in our study with the CFS cores (Figures S5A and S5B). Closer scrutiny of the experimental conditions in CFS studies led us to conclude that this apparent discrepancy stemmed from the differential usage of organic solvent for APH (i.e., ethanol versus DMSO; see Discussion). However, we did observe significant correlation between replication stress-induced DSBs in NM and FX cells with the APH.breakome ( $p < 0.001$ , Figure S5C).

CFSs have been characterized by late replication timing (Hellman et al., 2000; Le Beau et al., 1998; Palakodeti et al., 2004; Wang et al., 1999). Therefore, we asked whether the APH-induced DSBs in our study were located in late-replicating sequences. Using published Repli-seq data for GM06990 cells (Hansen et al., 2010), we divided the genome into 50-kb early- or late-replicating segments and calculated the percentage of DSBs in each segment. The majority of DSBs (at least 60%) were associated with late-replicating sequences in all samples (Figure 4D). In addition, the concordant DSBs (those that were shared between our data and the APH.breakome) were similarly associated with the late-replicating regions for both NM and FX cells (Figure S5D,  $p < 10E-3$ ). A subset of the concordant DSBs with the APH.breakome sites was also associated with early-replicating regions, highlighting a mechanism of DSB formation that is independent of the late-replication timing archetype (Figure S5E,  $p < 10E-3$ ). This observation is reminiscent of a previous study that reported early-replicating fragile sites in actively transcribing genes in B cells challenged with hydroxyurea, which induces replication stress by limiting the nucleotide pool (Barlow et al., 2013).

Therefore, we next inspected the distribution of DSBs with respect to genes. Approximately 30%–40% of DSBs in all of the samples occurred in genic regions with a dominant presence in introns. NM cells had 33% of spontaneous DSBs (from

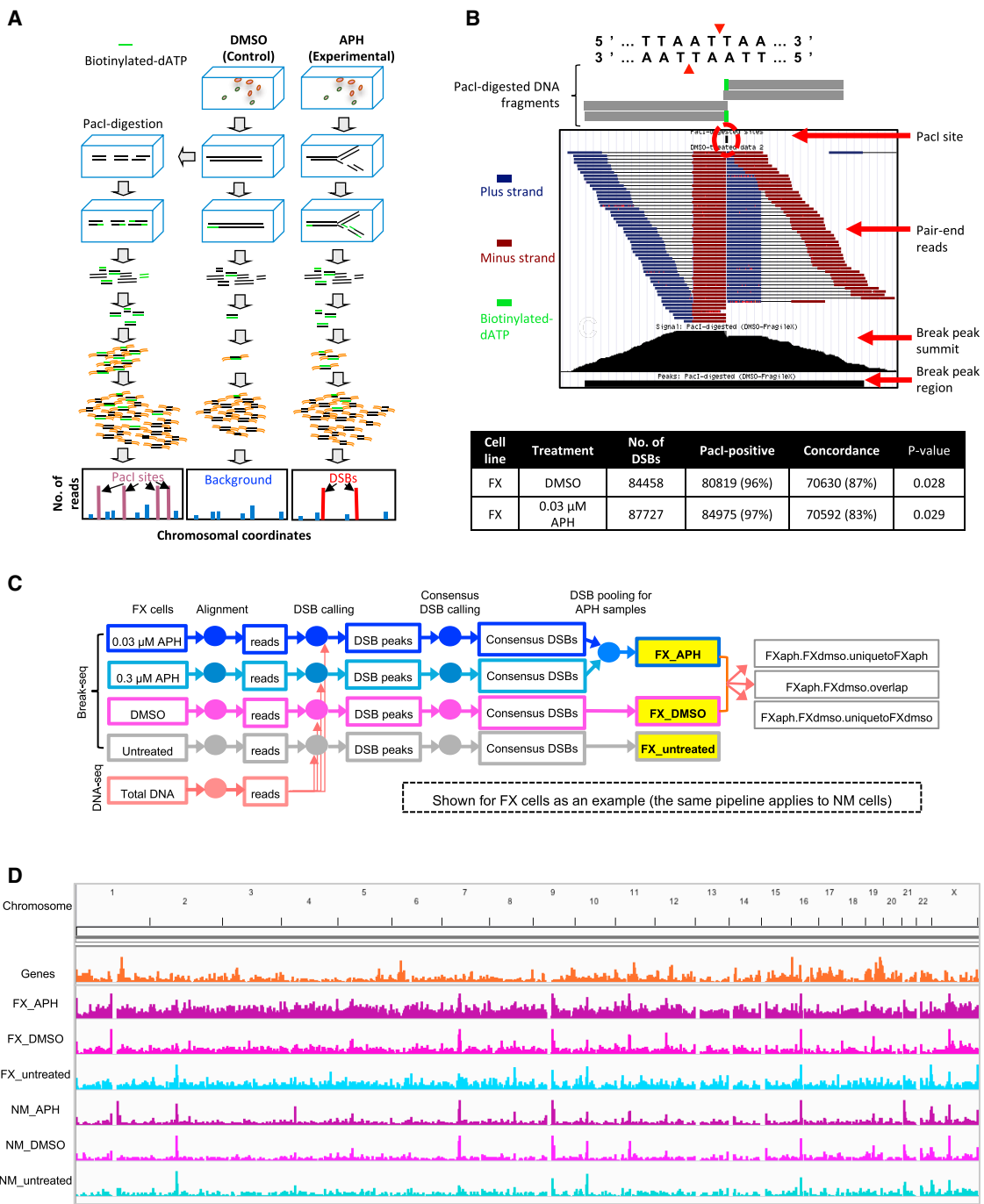


### Figure 3. DSB Mapping by Break-Seq in Lymphoblastoid Cells

### (A) Break-seq workflow.

(B) Break-seq sample read pile-up of a *PacI* site leading to the identification of a “peak” in the “proof-of-principle” experiment. The table denotes total *PacI* sites identified in DMSO-treated and (0.03  $\mu$ M) APH-treated FX cells.

(C) Schematic for Break-seq analysis. The sequence reads were aligned with Bowtie2, followed by model-based analysis of ChIP-seq 2 (MACS2) peak calling while normalizing for copy-number variation by whole-genome sequencing (“total DNA”) for NM and FX cells, respectively (shown for FX cells only). DSB peaks found in at least 2 replicate experiments for each strain/treatment combination were identified as “consensus DSBs” by DiffBind. Peaks from different APH treatments (0.03 and 0.3  $\mu$ M) were then pooled into a single set of “FX\_APH” DSBs, in contrast to the control datasets. The consensus DSBs for each strain/treatment combination were compared with each other (e.g., between “FX\_APH” and “FX\_DMSO”) to identify overlaps and condition-specific DSBs, ready for further comparison with genomic features such as RLFSS.

(D) Whole-genome distribution of DSBs in the indicated categories.

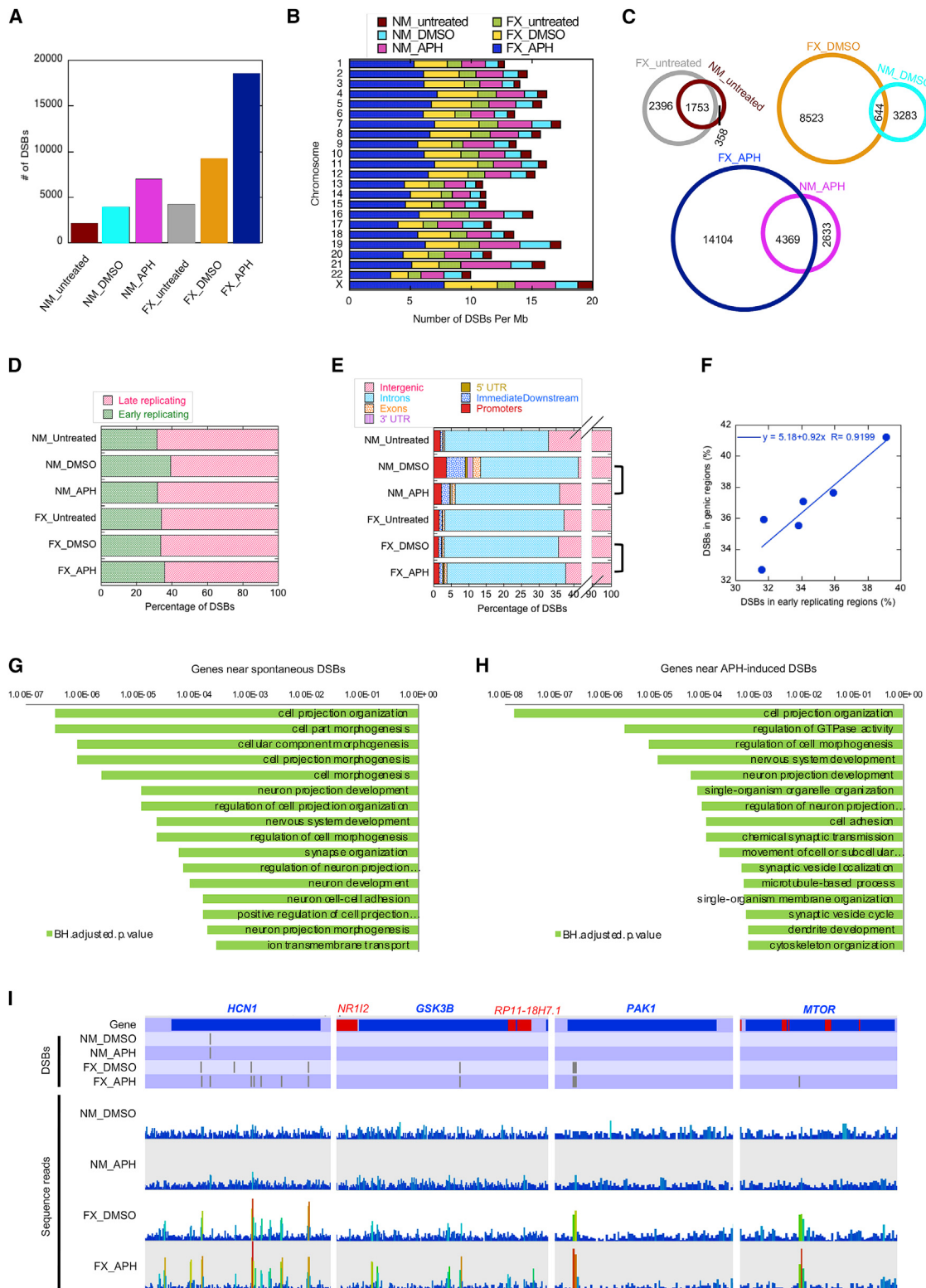


**Figure 4. DSB Association with Genomic Features**

(A) Plot of total number of DSBs in each of the indicated categories.

(B) DSB density (per megabase of DNA) across each chromosome for the indicated categories.

(C) Venn diagrams compare concordance between NM and FX cells for every treatment.

(legend continued on next page)

untreated cells) within genes, compared to 37% for FX cells. We do not know whether this increase in genic association for DSBs in FX cells is related to the higher level of transcription in FX cells. However, it has been shown that FMRP knockout mouse neurons exhibit increased gene expression compared to control neurons (Korb et al., 2017). Vehicle treatment increased the genic association to 41% for DSBs in NM cells, followed by a return to 36% with APH (Figure 4E). In contrast, FX cells showed a constant level of DSB-gene association, with 36% and 38% in vehicle- and APH-treated conditions, respectively (Figure 4E). The percentage of DSBs that fall in the early-replicating regions is correlated with the percentage of DSBs within genes (Figure 4F). These results suggest two types of APH-induced chromosome breakage—those in the intergenic regions that undergo delayed replication and those in the gene-rich early-replicating regions that may experience elevated levels of gene transcription. We also asked whether our DSBs are enriched in large genes that have been suggested to correspond to late-replicating CFSs. We used a published dataset of t-SDRs and t-SDWs, corresponding to “significantly delayed regions” and “significantly delayed windows” that each contain large (>300 kb) transcribed genes (Brison et al., 2019). We did observe a positive, although not statistically significant, correlation between drug-induced DSBs in FX cells with t-SDWs (Figure S5F). In contrast, the APH.breakome did not demonstrate correlation with these domains with large genes (Figure S5G).

Next, we annotated the genes neighboring spontaneous DSBs within a 5-kb maximal distance. For DSBs in NM cells, there was no significant ( $p < 0.001$ ) GO (Gene Ontology) enrichment. In contrast, spontaneous DSB-associated genes in FX cells were enriched in “neuron projection development,” “synapse organization,” and “neuron cell-cell adhesion” (Figure 4G). This result suggested that neuronal developmental genes were susceptible to chromosome breakage in the FX background, even without replication stress. Moreover, APH treatment further enhanced the GO enrichment in the same pathways (Figure 4H). A complete list of pathways associated with DSBs in all of the samples is shown in Table S2. Notably, many genes previously validated as FMRP-binding mRNAs such as *HCN1*, *GSK3B*, *PAK1*, and *MTOR*, showed specific DSB formation in FX cells (Figure 4I). This result indicated that FMRP, in addition to regulating the mRNA translation of its target genes, also maintains the stability of genomic loci where these genes reside.

### Preferential Association between Drug-Induced DSBs and RLFS in FX Cells

If the gene-associated DSBs were due to drug-induced replication-transcription conflict at actively transcribing genes, DSBs

may correlate with R-loops, which are co-transcriptional structures. We surveyed a database of RLFSs predicted by a previously described algorithm (Wongsurawat et al., 2012) for correlation with DSBs in a Fisher’s exact test (Table S3, small right tail p value indicates more overlaps than expected from a random simulation test and is used for reporting below). Untreated cells did not show enrichment of spontaneous DSBs at RLFSs; however, DMSO-treated NM and FX cells both showed significant enrichment of DSBs at RLFSs ( $p = 1.22E-34$  and  $3.71E-37$  with enrichment ratios of 1.746 and 1.493, respectively). Notably, DSBs in APH-treated NM cells were no longer enriched at RLFSs ( $p = 0.96$  with an enrichment ratio of 0.927), whereas those in APH-treated FX cells remained associated with RLFSs ( $p = 1.25E-66$  with an enrichment ratio of 1.498). These results were corroborated by the absolute distance measurements between DSBs and RLFSs (Table S4) using GenometriCorr (Favorov et al., 2012). We concluded that (1) DMSO elicits transcriptional response, possibly through oxidative stress (see Discussion), in both NM and FX cells and causes DSBs at RLFSs within actively transcribing genes, and (2) replication inhibition by APH triggers NM cells to deploy a mechanism to protect genes from DSBs at RLFSs, whereas FX cells lacked such a mechanism. Consistent with our interpretations, we note that in comparing the vehicle- and APH-treated samples, NM cells underwent a decrease from 41% to 36% in DSB-gene association, whereas FX cells showed the opposite trend, increasing from 36% to 38% (Figure 4E, brackets). In fact, APH-specific DSBs in FX cells (DSB group “FXdms0.FXaph.uniquetoFXaph”) showed the greatest association with genes (58.8%) compared to DSBs in any other category (Table S5). The aggregated distribution of DSBs around RLFSs showed an enrichment of DSBs immediately downstream of the RLFS start and immediately upstream of the RLFS end, specifically in the drug-treated FX cells (Figures 5A and 5B). Overall, these results led us to conclude that FX cells form DSBs at RLFSs when treated with DMSO, a response that is further enhanced by APH. We also compared the DSBs to a composite list of DRIP-seq (DNA:RNA hybrid immunoprecipitation followed by sequencing) signals, generated by merging all DRIP-seq signals in NT2 and K562 cell lines to minimize cell-type-specific differences (Sanz et al., 2016). The results largely recapitulated the comparison between DSBs and RLFSs (Table S3).

The strong correlation between DSBs and RLFSs in FX cells is most pronounced on chromosomes 1, 13, 14, 15, 21, and 22, which contain rDNA clusters, followed by chromosomes 2, 6, and 12 (Table S4). Notably, the DSBs on the rDNA-bearing chromosomes were not confined to the rDNA loci. We used immunofluorescence to validate that FX cells accumulate R-loops or RNA:DNA hybrids upon replication stress using the S9.6

(D) Distribution of DSBs in early- versus late-replicating regions of the genome, as defined by Hansen et al. (2010) in the indicated samples (see Method Details). (E) Distribution of DSB peaks relative to genes in the indicated samples. Genic features include introns, exons, 5'- and 3' UTRs, promoters, and the immediately downstream (<1 kb from the 3' UTR) regions (ImmediateDownstream). Note the break in the x axis to show all of the genic features.

(F) Correlation between DSBs associated with genes and with early-replication timing sequences.

(G and H) Gene Ontology (GO) terms for genes associated with DSBs in FX-untreated (G) and APH-treated (H) samples. Plotted are the BH (Benjamini-Hochberg) adjusted p values for the GO terms.

(I) Examples of genes containing drug-induced DSBs specifically in the FX cells. The top tier of the plots annotate the DSB positions in genes labeled red or blue for Watson- or Crick-strand-encoded, respectively. The bottom tier show sequence read distribution in each data track, with increasing numbers following a blue to red color scale.

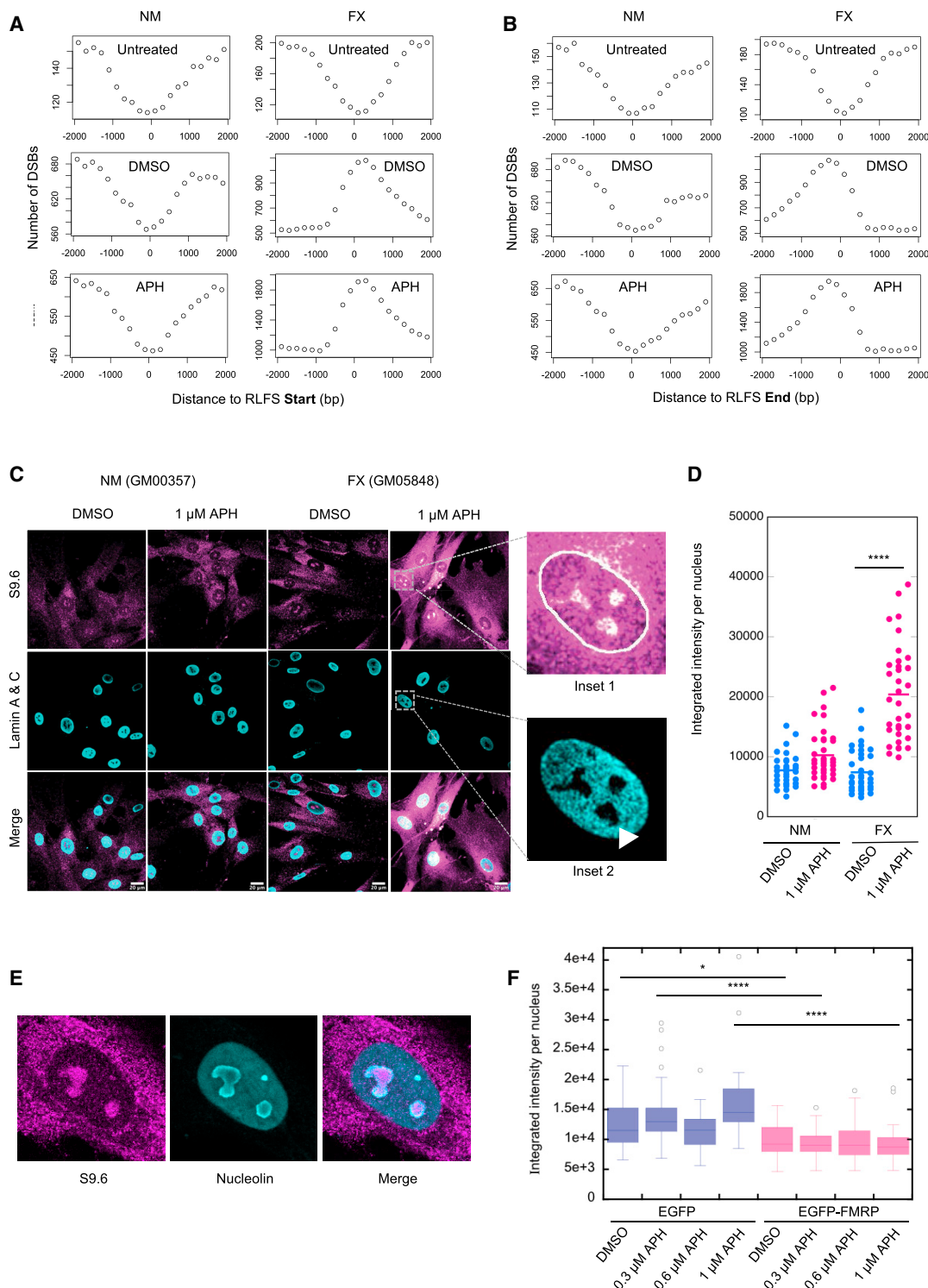


**Figure 5. DSB Correlation with RLFSs and Increased RNA:DNA Hybrids in FX Cells In Vivo**

(A and B) Aggregated DSBs from the indicated samples around the start (A) or the end (B) of RLFS in a 4,000-bp window centering on the RLFS. (C) Confocal images of immunofluorescence staining with the S9.6 antibody. The nuclear boundary is traced by Lamin staining (inset 1). The RNA:DNA hybrid signals are enriched in the areas of the nucleus lacking DAPI staining, which are presumed the nucleoli (arrowhead in inset 2). Scale bar, 20  $\mu$ m. (D) Quantification of nuclear S9.6 signals in two independent experiments ( $n \geq 33$  in each) using one-way ANOVA with multiple comparisons. \* $p < 0.0001$ .

(legend continued on next page)

antibody. RNA:DNA hybrid signals in the nucleus were significantly increased upon APH treatment compared to vehicle-treated sample in FX cells, in contrast to a moderate increase in NM cells (Figures 5C and 5D). Moreover, the RNA:DNA foci appeared to be enriched in areas of the nucleus that were devoid of DAPI stain, which were characteristic of the nucleoli (Figure 5C, insets). We confirmed this finding using nucleolin co-staining with S9.6 antibody (Figure 5E). This result supported the notion that DSBs showed preferential association with RLFSs on the nucleolar resident chromosomes. Finally, we demonstrated that the ectopic expression of EGFP-FMRP also reduced the RNA:DNA hybrid levels in the FX cells (Figure 5F). Of note, the S9.6-detected signals were labile to RNase H treatment, suggesting that they corresponded to RNA:DNA hybrids (Figures S6A and S6B). Therefore, we hypothesized that FMRP is required for R-loop prevention during replication stress.

#### Ectopic Expression of FMRP, but Not the FMRP-I304N Mutant, Reduces RLFS-Induced DSBs

To test whether FMRP prevents R-loop formation, we used a modified yeast-based recombination assay (Prado and Aguilera, 2005) to measure DSB frequency in programmed transcription-replication conflict induced by human RLFSs (Figure 6A). We chose this model system for its simplicity and perspicuity. By co-expressing human RLFSs and FMRP, for which there is no known yeast ortholog, we were able to specifically analyze the interaction between these entities. In the absence of RLFS insertion, there was a 4.7-fold enhancement of recombination frequency (RF) on the plasmid with convergent replication and transcription compared to a co-directional configuration (Figure S7A), consistent with the previous observation (Prado and Aguilera, 2005). Two human RLFSs, when inserted in the sense direction, each caused elevated RF over the control sequence (non-RLFS), in the convergent replication-transcription configuration specifically (2- and 4-fold,  $p = 0.0024$  and  $p < 0.0001$ , respectively; Figure S7B). RF was further enhanced in a strain lacking RNase H1, an enzyme known to resolve R-loops by degrading the RNA:DNA hybrid: ~2- and 1.5-fold for sense and anti-sense orientation, respectively, for RLFS-1, and ~1.2-fold for both sense and anti-sense orientations, for RLFS-2 (Figures S7B and S7C). Because RLFS-2 already induced high RF, further enhancement by eliminating RNase H1 was only moderate. Next, we asked whether ectopic expression of FMRP would decrease RLFS-induced DSBs. The expression of empty vector did not alter the RLFS-induced RF (comparing Figure S7B to Figure S7D). A significant decrease in RF was observed for the expression of FMRP (2- and 1.6-fold for RLFS-1 and RLFS-2, respectively) or a positive control, RNase H1, but not for a non-specific RNA-binding protein, She2, compared to empty vector (Figure 6B). Finally, a mutant FMRP containing an I304N substitution in the KH2 domain, a rare *de novo* mutation that led to FXS (De Boulle et al., 1993; Siomi et al., 1994), no longer suppressed RF (Figure 6B). We also verified that FMRP and FMRP-I304N

showed similar levels of protein expression in yeast (Figure S7E). The I304N mutation abolishes FMRP binding to mRNA and the polysome (Feng et al., 1997). Our results thus suggest that the KH2 domain is also involved in interactions with R-loops.

## DISCUSSION

#### FX Cells Are Intrinsically Unstable and More Susceptible to Replication Stress-Induced Chromosome Breakage on a Genome-wide Scale

The main discovery from our study is the inherent genome instability in FX cells. Our study marks the first demonstration of genome-wide chromosomal breakage in FX cells, with or without replication stress by APH. This represents a development in our understanding of FXS biology. FX cells were molecularly characterized by a fragile site called FRAXA at the *FMR1* locus on the metaphase chromosome, specifically induced by folate stress, in individuals with full mutation of the CGG repeat expansion. While there were abundant studies measuring FRAXA site expression, relatively few compared the number of CFSs induced by APH in FX cells to controls. One study reported a >3-fold increase in the CFS frequencies in FX patients (27.9%) compared to unaffected controls (7.9%) when their cells were treated with APH (Murano et al., 1989). This result is consistent with our observation of the >2-fold increase in DSBs in FX cells compared to controls. The global induction of DSBs in the FX genome also corroborated the observed increased DSB formation assayed by  $\gamma$ H2A.X staining and Comet assay. It is noteworthy that our observation of increased  $\gamma$ H2A.X staining in human FXS patient-derived cells contrasts the reduced  $\gamma$ H2A.X staining in *fmr1*<sup>-/-</sup> mouse embryonic fibroblasts (Alpatov et al., 2014). Moreover, we observed a robust DDR in the FX cells in response to APH, also contrary to the reported deficiency in DDR in the FX mouse model (Alpatov et al., 2014). Our study thus revealed fundamental differences between the human cells from FXS and those from the mouse model. However, we note that the ATM protein level in the untreated conditions is lower in the FX cells relative to the control, consistent with a previous report of decreased expression of DNA repair genes in the FX patients (Xu et al., 2013). Therefore, future investigation into how changes in the gene expression of the DNA repair pathway directly affects genome stability in FX cells would be warranted.

The comparison between our DSBs and previously identified core sequences of CFSs did not yield a statistically significant correlation. We believe this was at least partially due to the differential usage of solvents for APH in the literature. Since the first documented usage of ethanol and DMSO as solvents for APH in inducing CFSs (Glover et al., 1984), different laboratories have taken to use either solvent for their studies. To the best of our knowledge direct comparison of DMSO and APH has only been documented in a single study using two subjects (Kuwano and Kajii, 1987). Unfortunately, the effect of DMSO alone on CFS induction was not measured. Among the studies in which the

(E) Validation of the co-localization of RNA:DNA hybrids with nucleolus by co-staining with S9.6 and anti-nucleolin. Shown is an example of DMSO-treated FX cells. Similar observations were made with APH-treated cells (data not shown).

(F) Nuclear S9.6 signals were reduced by the ectopic expression of EGFP-FMRP, compared to the EGFP control, in FX cells. Quantification was done similarly as in (D). \* $p < 0.05$  and \*\*\* $p < 0.0001$ .

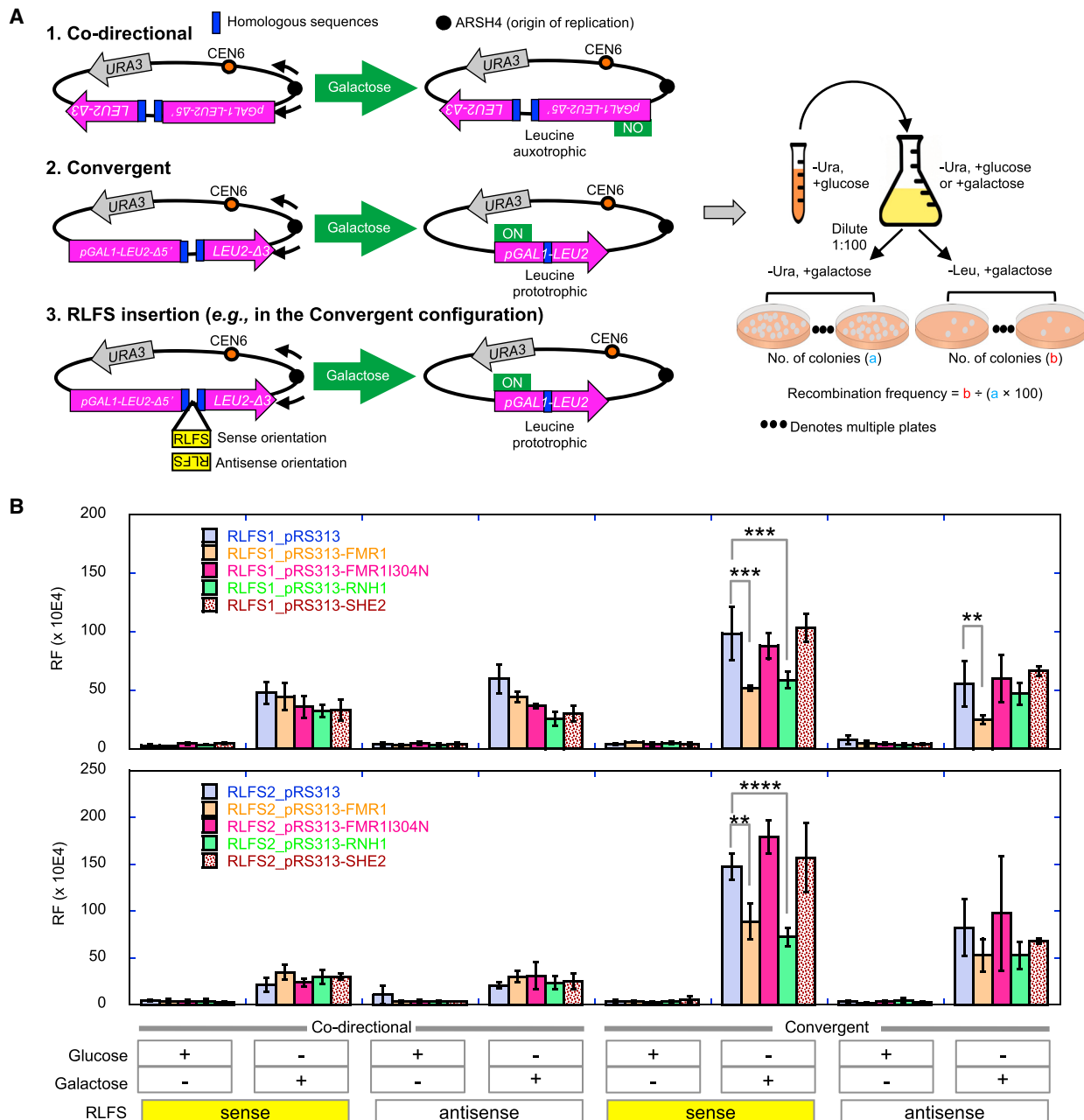


**Figure 6. FMRP Expression Suppresses RLFS-Induced DSB Formation**

(A) A non-functional *LEU2* marker containing 2 inserted direct repeats and driven by a galactose-inducible *GAL1* promoter was placed next to an origin of replication (*ARSH4*), such that the direction of transcription is convergent or co-directional with respect to the direction of the proximal replication fork. Upon galactose induction, convergent replication and transcription would induce DSBs and homologous recombination repair to generate a functional *LEU2*, resulting in leucine prototrophy. Two RLFSs from the human genome (RLFS1-1 from the promoter of *FMR1* and RLFS-2 from intron 5 of the fragile histidine triad) were inserted between the direct repeats to test for enhanced DSB and recombination. A non-RLFS sequence without predicted R-loop forming propensity and with similar G-richness in both strands served as the control. All of the sequences were similar in size (~500 bp). The RLFSs were inserted in the sense or anti-sense orientation with respect to *LEU2* transcription (i.e., G-rich strand on the non-template or template strand, respectively), with the sense orientation expected to preferentially induce R-loop formation. The control sequence was also inserted in two orientations, and no difference in RF was observed between them (see Figure S5C). RF is calculated based on the percentage of leucine prototrophs after plating.

(B) The effect of ectopic expression of indicated genes on the pRS313 plasmid, under the cytomegalovirus (CMV) promoter, on RLFS-induced RF. Error bars indicate standard deviation. \*\* $p < 0.01$ , \*\*\* $p < 0.001$ , and \*\*\*\* $p < 0.0001$ .

See Figure S7 for additional control experiments.

CFS core sequences were derived (Savelyeva and Brueckner, 2014), all but one study used ethanol. The study by Zimonjic et al. (1997) used either ethanol or DMSO to map FRA3B and the results were an undifferentiated mixture. The study by Le Tallec et al. (2013) did not indicate the solvent used. Notably, the DSBs in our study showed significant correlation with those identified by another DSB mapping method (BLESS) (Crosetto et al., 2013). Both studies used DMSO as the solvent. Therefore, it appears that CFS formation is a product of both APH and other undefined cellular effects by ethanol or DMSO, rendering comparison between studies that have differential usage of solvent rather tenuous. Our study showed that DMSO sensitizes RLFS regions for DSBs in both NM and FX cells. DMSO is one of the most common solvents for organic compounds and facilitates the delivery of drugs across cellular membranes. It is also known as an antioxidant with a protective role for human tissues by interacting with the hydroxyl group on various substances. However, depending on the concentration and cellular context, DMSO can function as an antioxidant or a pro-oxidant (Kang et al., 2017; Liu et al., 2001; Pérez-Pastén et al., 2006; Sadowska-Bartosz et al., 2013). We discovered that 0.02% DMSO can cause chromosome breakage, at least in human lymphoblastoids, through an unknown mechanism. Thus, it is imperative to understand the full cellular and genomic impact by DMSO to inform drug treatment involving DMSO as a solvent.

### A Role for FMRP in Preventing R-Loop Formation during Replication Stress

Our study also provided an explanation for why the FX genome is inherently unstable. We showed that there are two types of DSBs in FMRP-deficient FX cells: those occurring in both control and FX cells in gene-poor regions with delayed replication timing and those occurring specifically in FX cells near RLFSs within genes. The latter suggests that FMRP plays a role in preventing R-loop formation during replication-transcription conflicts. We demonstrated that FX cells accumulate R-loops upon replication stress. We then homed in on those “at-risk” genes that harbor DSBs in the FX genome and found them to be enriched in the neuronal differentiation and synapse organization pathways, linking genomic instability to the FXS pathology. The notion that replication-transcription conflict underlies defective neuronal gene expression presents an apparent conundrum that neurons are predominantly postmitotic cells. However, we reckoned the following. FX patients usually develop signs of ID such as delayed speech by the age of 2 years, shortly after new neuronal growth stops at ~18 months. This suggests that FMRP deficiency may affect neurogenesis during a period of mitotic growth with active replication and gene expression. In addition, neurogenesis continues to occur in adult brain regions such as the hippocampus, and specifically, the dentate gyrus (Boldrini et al., 2018; Curtis et al., 2012; Eriksson et al., 1998; Kempermann et al., 2015). ID in FX is thought to be due to dysregulated synaptic plasticity in the hippocampus, and FMRP expression is enriched in the dentate gyrus and field CA1 neuronal cells in the hippocampus, among other regions of the mouse brain (Zorio et al., 2017). Moreover, FMRP is also expressed in glial cells such as astrocytes of the developing central nervous system in mice. These cells are important regulators of neuronal develop-

ment in FX. Studies have shown that hippocampal neurons from a normal mouse displayed abnormal dendritic morphology when co-cultured with astrocytes from a mouse with FMRP deficiency, and this phenotype was rescued by normal astrocytes (Jacobs et al., 2016). Finally, our results indicate that not all DSBs in FX cells are induced as a result of replication-transcription conflict.

Many of the “at-risk” genes in FX cells were previously identified as mRNA substrates regulated by FMRP on the polysomes. These results led us to hypothesize that FMRP binds to its gene substrates on the chromatin during transcription, before transporting the mRNAs to the ribosomes for translation. We observed that DMSO or APH caused DSBs to gravitate toward RLFSs in FX cells, whereas only DMSO, not APH, elicited the same response in NM cells. The implications for these results are 2-fold. First, they suggest that DMSO induces a strong transcriptional response and can cause DSBs at RLFSs. Second, replication stress by APH activates FMRP and lowers the incidence of DSBs at RLFSs compared to DMSO in NM cells. Hence, in the absence of FMRP, FX cells fail to protect their genome upon replication stress. This notion is supported by the observation that ectopic expression of FMRP reduced DNA damage in FX cells. These results are consistent with an FMRP function in genome maintenance, particularly during replication stress.

However, we do not believe FMRP interacts with the replication fork directly. In fact, we have not found any evidence for FMRPs associating with replication forks from the literature. Instead, our results suggest a scenario in which FMRP interacts with transiently formed R-loops during transcription and facilitates the passaging of replication forks traversing toward the transcription machinery so as to prevent chromosome breakage. This previously unknown function of FMRP is supported by its ability to suppress RLFS-induced recombination during programmed replication-transcription conflict, which is dependent on its KH2 RNA-binding domain. This function is also consistent with the known affinity of FMRP for RNA, single-strand DNA (ssDNA), and dsDNA (Ashley et al., 1993), three substrates that are all present in an R-loop. Alternatively, FMRP can mediate R-loop formation by forming complex with other R-loop interacting proteins. For instance, FMRP can form complex with DNA topoisomerase III  $\beta$  (TOP3B) and Tudor domain-containing protein 3 (TDRD3), which have been shown to prevent R-loop formation at cMYC/immunoglobulin DSB sites (Nott and Tsai, 2013). FMRP was also reported to interact with the THO/TREX (suppressors of the transcription defects of *hpr1* $\Delta$  mutants by overexpression-Transcription and Export) complex, a messenger ribonucleoprotein (mRNP) transporter known to be involved in R-loop prevention (Dominguez-Sánchez et al., 2011), through affinity purification (Hein et al., 2015). Finally, the DSBs in FX cells might be triggered by the dysregulated expression of nucleases such as MUS81, ERCC1, and XPF, independent of R-loop formation (Chappidi et al., 2020; Matos et al., 2020; Naim et al., 2013; Ying et al., 2013).

### A Potential Mechanism Linking Increased Protein Synthesis to Genome Instability in the Absence of FMRP

Our data suggested that RNA:DNA hybrids localized to dark areas of the nucleus, likely the nucleolus, in FX cells. These results are consistent with the observed correlation between DSBs and RLFSs, preferentially occurring on rDNA-bearing

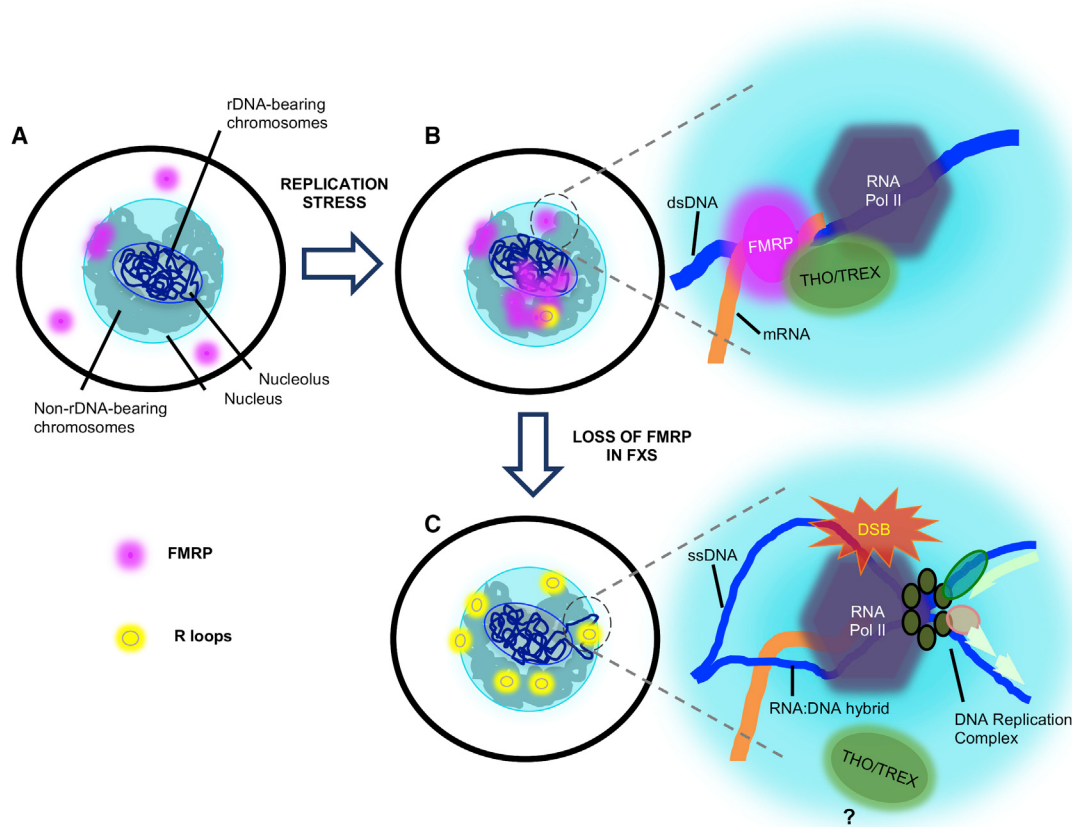


**Figure 7. Proposed Model for FMRP R-Loop Regulation and DSB Prevention**

(A) Illustration of a normal cell without any treatment, showing FMRP in the cytoplasm and in the nuclear periphery, possibly engaged in mRNA transport.  
 (B) Under replication stress induced by DMSO and APH, FMRP increases its presence in the nucleus. At the junction of replication and transcription collision, FMRP, in conjunction with R-loop processing factors such as the THO-TREX complex, is involved in R-loop removal and avoidance of a deleterious collision (inset). dsDNA, double-stranded DNA.  
 (C) In FX cells, increased protein synthesis rate demands high-level rRNA production on the rDNA-bearing chromosomes, which in turn causes increased levels of (RNA Pol II) transcription elsewhere on these chromosomes, represented by the chromosome loops tethered to the nuclear pores for active transcription. The absence of FMRP permits stable R-loop formation and DSBs upon the collision of replication and transcription (inset). ssDNA, single-strand DNA.

chromosomes, which are residents of the nucleolus. Are rDNA-bearing chromosomes prone to DSBs simply by virtue of being proximal to the nucleolus as a locale, or is there an underlying cause for these chromosomes to generate RLFS-associated DSBs? We favor the latter explanation. While the 45S rDNA array residing on the short arms of five acrocentric chromosomes (13, 14, 15, 21, and 22) defines the nucleolus, the 5S rDNA array is a resident of chromosome 1 and the 5S and 45S rDNA arrays are not in close proximity spatially in human lymphoblastoid cells (Yu and Lemos, 2016). This suggests that DSB-RLFS association on these chromosomes is not mediated by proximity to the nucleolus per se. Instead, we reason that the act of transcription on the chromosomes containing 45S rDNA subjects them to increased R-loop formation and chromosome breakage. FMRP deficiency leads to elevated levels of protein translation (Darnell et al., 2011), which would be reliant on an increased rate of ribosome production. Therefore, we hypothesized that FX cells, to sustain high levels of rRNA transcription, relay the stress, likely torsional in nature, from the rDNA loci intrachromosomally onto

the remainder of the chromosome, causing heightened replication-transcription conflicts and chromosome breakage.

In summary, our study led us to a model in which FMRP guards its gene substrates from the nucleus to the cytoplasm (Figure 7). While its main function is a translation regulator on the polyribosomes, FMRP increases its nuclear presence to prevent R-loop formation and chromosome breakage during heightened replication-transcription conflicts. We note that FX cells also produce spontaneous DSBs at a higher level than NM cells, and these spontaneous DSBs are not correlated with RLFSs. This suggests that FMRP has additional protective role(s) toward the genome without external replication stress. Recent studies have shown that FMRP deficiency causes an imbalance of epigenetic modifications due to unregulated protein synthesis (Korb et al., 2017; Li et al., 2018). It is plausible that the spontaneous chromosome breakage in FX cells is a result of altered histone modifications that predispose specific regions of the chromatin to breakage. Together with our discovery that FMRP directly interacts with the chromatin (data not shown), these

attributes make FMRP a mediator of transcription and replication to prevent R-loop accumulation and ensure genome integrity, thereby maintaining synaptic plasticity in neuronal cells.

## STAR★METHODS

Detailed methods are provided in the online version of this paper and include the following:

- **KEY RESOURCES TABLE**
- **RESOURCE AVAILABILITY**
  - Lead Contact
  - Materials Availability
  - Data and Code Availability
- **EXPERIMENTAL MODEL AND SUBJECT DETAILS**
  - Cell line growth and culture conditions
  - Yeast strains
- **METHOD DETAILS**
  - Cell line drug treatment conditions
  - Cloning
  - Lentiviral-assisted cell transfection
  - Flow cytometry for cell cycle analysis
  - Flow cytometry for quantification of cells stained for γH2A.X
  - Immunocytochemistry and microscopy
  - Single cell gel electrophoresis assay
  - Break-seq library construction
  - Western blot
  - Yeast strains and plasmids
  - Recombination frequency assay
  - Gene ontology analysis and identification of pathways that are potentially altered by treatment
- **QUANTIFICATION AND STATISTICAL ANALYSIS**
  - Break-seq DSB peak identification
  - Random permutation tests for identification of Pacl sites
  - Break-seq library complexity calculation and identification of consensus DSB peaks in replicate experiments
  - Correlation between DSBs and other genomic features
  - Calculation of replication timing for DSB regions
  - Genomic association tests for correlation between DSBs and CFS cores and the “APH.breakome.”
  - Statistical analysis

## SUPPLEMENTAL INFORMATION

Supplemental Information can be found online at <https://doi.org/10.1016/j.celrep.2020.108179>.

## ACKNOWLEDGMENTS

We thank V. Van Steenkist for systems support; Drs. L. Kotula, C. Dobkin, B. Howell, and A. Aguilera for antibodies and plasmids; and Drs. L. Kotula, F. Middleton, P. Kane, and T. Wongsurawat for helpful discussions. We also thank the staff at SUNY Upstate Flow Cytometry Core and the University at Buffalo Genomics Core for flow sorting and HiSeq sequencing, respectively. This work was supported by the National Institutes of Health grants 5R00GM08137805 and 5R01-GM118799 to W.F.; the Department of Defense CDMRP Discovery Award W81XWH-15-1-0204 to W.F.; institutional support from A\*STAR and a

SUNY EMPIRE scholar grant to V.A.K.; the Department of Defense grant PC160083 to H.H.; the I. Curie YPI program, the ATIP-Avenir program from CNRS and Plan Cancer from INSERM, and the Agence Nationale pour la Recherche (ANR) to C.L.C.; and the National Institutes of Health grant 5R01-GM045751 to C.S.

## AUTHOR CONTRIBUTIONS

A.C. and W.F. conceived the study and designed the experiments. A.C., A.M., E.A.H., B.H., A.B., and W.F. performed the Break-seq experiments. A.C., J.L., and H.H. performed and analyzed the immunostaining experiments. A.C. and A.T. performed the recombination assays. A.C. performed and analyzed the flow cytometry. P.J., V.A.K., S.E.H., C.L.C., and W.F. performed the computational analyses. C.S. provided intellectual contributions over many discussions on fragile sites. A.C. and W.F. wrote the manuscript with input from all of the authors.

## DECLARATION OF INTERESTS

The authors declare no competing interests.

Received: March 19, 2020

Revised: July 17, 2020

Accepted: August 31, 2020

Published: September 22, 2020

## REFERENCES

- Alpatov, R., Lesch, B.J., Nakamoto-Kinoshita, M., Blanco, A., Chen, S., Stützer, A., Armache, K.J., Simon, M.D., Xu, C., Ali, M., et al. (2014). A chromatin-dependent role of the fragile X mental retardation protein FMRP in the DNA damage response. *Cell* 157, 869–881.
- Ashley, C.T., Jr., Wilkinson, K.D., Reines, D., and Warren, S.T. (1993). FMR1 protein: conserved RNP family domains and selective RNA binding. *Science* 262, 563–566.
- Barlow, J.H., Faryabi, R.B., Callén, E., Wong, N., Malhowski, A., Chen, H.T., Gutierrez-Cruz, G., Sun, H.W., McKinnon, P., Wright, G., et al. (2013). Identification of early replicating fragile sites that contribute to genome instability. *Cell* 152, 620–632.
- Bear, M.F., Huber, K.M., and Warren, S.T. (2004). The mGluR theory of fragile X mental retardation. *Trends Neurosci.* 27, 370–377.
- Boldrini, M., Fulmore, C.A., Tatt, A.N., Simeon, L.R., Pavlova, I., Poposka, V., Rosoklja, G.B., Stankov, A., Arango, V., Dwork, A.J., et al. (2018). Human Hippocampal Neurogenesis Persists throughout Aging. *Cell Stem Cell* 22, 589–599.e5.
- Brison, O., El-Hilali, S., Azar, D., Koundrioukoff, S., Schmidt, M., Nähse, V., Jaszczyzyn, Y., Lachages, A.M., Dutrillaux, B., Thermes, C., et al. (2019). Transcription-mediated organization of the replication initiation program across large genes sets common fragile sites genome-wide. *Nat. Commun.* 10, 5693.
- Brown, V., Jin, P., Ceman, S., Darnell, J.C., O'Donnell, W.T., Tenenbaum, S.A., Jin, X., Feng, Y., Wilkinson, K.D., Keene, J.D., et al. (2001). Microarray identification of FMRP-associated brain mRNAs and altered mRNA translational profiles in fragile X syndrome. *Cell* 107, 477–487.
- Chappidi, N., Nascakova, Z., Boleslavská, B., Zellweger, R., Isik, E., Andrs, M., Menon, S., Dobrovolna, J., Balbo Pogliano, C., Matos, J., et al. (2020). Fork Cleavage-Religation Cycle and Active Transcription Mediate Replication Restart after Fork Stalling at Co-transcriptional R-Loops. *Mol. Cell* 77, 528–541.e8.
- Chen, C.L., Rappailles, A., Duquenne, L., Huvet, M., Guilbaud, G., Farinelli, L., Audit, B., d'Aubenton-Carafa, Y., Arneodo, A., Hyrien, O., and Thermes, C. (2010). Impact of replication timing on non-CpG and CpG substitution rates in mammalian genomes. *Genome Res.* 20, 447–457.
- Ciacio, C., Fontana, L., Milani, D., Tabano, S., Miozzo, M., and Esposito, S. (2017). Fragile X syndrome: a review of clinical and molecular diagnoses. *Ital. J. Pediatr.* 43, 39.

- Coffee, B., Zhang, F., Ceman, S., Warren, S.T., and Reines, D. (2002). Histone modifications depict an aberrantly heterochromatinized FMR1 gene in fragile X syndrome. *Am. J. Hum. Genet.* 71, 923–932.
- Crosetto, N., Mitra, A., Silva, M.J., Bienko, M., Dojer, N., Wang, Q., Karaca, E., Chiarle, R., Skrzypczak, M., Ginalski, K., et al. (2013). Nucleotide-resolution DNA double-strand break mapping by next-generation sequencing. *Nat. Methods* 10, 361–365.
- Curtis, M.A., Low, V.F., and Faull, R.L. (2012). Neurogenesis and progenitor cells in the adult human brain: a comparison between hippocampal and subventricular progenitor proliferation. *Dev. Neurobiol.* 72, 990–1005.
- Daley, T., and Smith, A.D. (2013). Predicting the molecular complexity of sequencing libraries. *Nat. Methods* 10, 325–327.
- Darnell, J.C., Van Driesche, S.J., Zhang, C., Hung, K.Y., Mele, A., Fraser, C.E., Stone, E.F., Chen, C., Fak, J.J., Chi, S.W., et al. (2011). FMRP stalls ribosomal translocation on mRNAs linked to synaptic function and autism. *Cell* 146, 247–261.
- De Boulle, K., Verkerk, A.J., Reyniers, E., Vits, L., Hendrickx, J., Van Roy, B., Van den Bos, F., de Graaff, E., Oostra, B.A., and Willems, P.J. (1993). A point mutation in the FMR-1 gene associated with fragile X mental retardation. *Nat. Genet.* 3, 31–35.
- Domínguez-Sánchez, M.S., Barroso, S., Gómez-González, B., Luna, R., and Aguilera, A. (2011). Genome instability and transcription elongation impairment in human cells depleted of THO/TREX. *PLOS Genet.* 7, e1002386.
- Entian, K.D., Schuster, T., Hegemann, J.H., Becher, D., Feldmann, H., Güldener, U., Götz, R., Hansen, M., Hollenberg, C.P., Jansen, G., et al. (1999). Functional analysis of 150 deletion mutants in *Saccharomyces cerevisiae* by a systematic approach. *Mol. Gen. Genet.* 262, 683–702.
- Erickson, C.A., Davenport, M.H., Schaefer, T.L., Wink, L.K., Pedapati, E.V., Sweeney, J.A., Fitzpatrick, S.E., Brown, W.T., Budimirovic, D., Hagerman, R.J., et al. (2017). Fragile X targeted pharmacotherapy: lessons learned and future directions. *J. Neurodev. Disord.* 9, 7.
- Eriksson, P.S., Perfilieva, E., Björk-Eriksson, T., Alborn, A.M., Nordborg, C., Peterson, D.A., and Gage, F.H. (1998). Neurogenesis in the adult human hippocampus. *Nat. Med.* 4, 1313–1317.
- Favorov, A., Mularoni, L., Cope, L.M., Medvedeva, Y., Mironov, A.A., Makeev, V.J., and Wheelan, S.J. (2012). Exploring massive, genome scale datasets with the GenometriCorr package. *PLOS Comput. Biol.* 8, e1002529.
- Feng, Y., Absher, D., Eberhart, D.E., Brown, V., Malter, H.E., and Warren, S.T. (1997). FMRP associates with polyribosomes as an mRNP, and the I304N mutation of severe fragile X syndrome abolishes this association. *Mol. Cell* 1, 109–118.
- Fu, Y.H., Kuhl, D.P., Pizzuti, A., Pieretti, M., Sutcliffe, J.S., Richards, S., Verkerk, A.J., Holden, J.J., Fenwick, R.G., Jr., Warren, S.T., et al. (1991). Variation of the CGG repeat at the fragile X site results in genetic instability: resolution of the Sherman paradox. *Cell* 67, 1047–1058.
- García-Rubio, M., Aguilera, P., Lafuente-Barquero, J., Ruiz, J.F., Simon, M.N., Geli, V., Rondón, A.G., and Aguilera, A. (2018). Yra1-bound RNA-DNA hybrids cause orientation-independent transcription-replication collisions and telomere instability. *Genes Dev.* 32, 965–977.
- Gerhardt, J., Tomishima, M.J., Zaninovic, N., Colak, D., Yan, Z., Zhan, Q., Rosenwaks, Z., Jaffrey, S.R., and Schildkraut, C.L. (2014). The DNA replication program is altered at the FMR1 locus in fragile X embryonic stem cells. *Mol. Cell* 53, 19–31.
- Glover, T.W., Berger, C., Coyle, J., and Echo, B. (1984). DNA polymerase alpha inhibition by aphidicolin induces gaps and breaks at common fragile sites in human chromosomes. *Hum. Genet.* 67, 136–142.
- Gyori, B.M., Venkatachalam, G., Thiagarajan, P.S., Hsu, D., and Clement, M.V. (2014). OpenComet: an automated tool for comet assay image analysis. *Redox Biol.* 2, 457–465.
- Hamperl, S., Bocek, M.J., Saldivar, J.C., Swigut, T., and Cimprich, K.A. (2017). Transcription-Replication Conflict Orientation Modulates R-Loop Levels and Activates Distinct DNA Damage Responses. *Cell* 170, 774–786.e19.
- Hansen, R.S., Thomas, S., Sandstrom, R., Canfield, T.K., Thurman, R.E., Weaver, M., Dorschner, M.O., Gartler, S.M., and Stamatoyannopoulos, J.A. (2010). Sequencing newly replicated DNA reveals widespread plasticity in human replication timing. *Proc. Natl. Acad. Sci. USA* 107, 139–144.
- Heger, A., Webber, C., Goodson, M., Ponting, C.P., and Lunter, G. (2013). GAT: a simulation framework for testing the association of genomic intervals. *Bioinformatics* 29, 2046–2048.
- Hein, M.Y., Hubner, N.C., Poser, I., Cox, J., Nagaraj, N., Toyoda, Y., Gak, I.A., Weisswange, I., Mansfeld, J., Buchholz, F., et al. (2015). A human interactome in three quantitative dimensions organized by stoichiometries and abundances. *Cell* 163, 712–723.
- Hellman, A., Rahat, A., Scherer, S.W., Darvasi, A., Tsui, L.C., and Kerem, B. (2000). Replication delay along FRA7H, a common fragile site on human chromosome 7, leads to chromosomal instability. *Mol. Cell. Biol.* 20, 4420–4427.
- Hoffman, E.A., McCulley, A., Haarer, B., Arnak, R., and Feng, W. (2015). Break-seq reveals hydroxyurea-induced chromosome fragility as a result of unscheduled conflict between DNA replication and transcription. *Genome Res.* 25, 402–412.
- Hoover, F. (2000). KaleidaGraph 3.5. *Science* 289, 1893.
- Huang, W., Sherman, B.T., and Lempicki, R.A. (2009). Systematic and integrative analysis of large gene lists using DAVID bioinformatics resources. *Nat. Protoc.* 4, 44–57.
- Jacobs, S., Cheng, C., and Doering, L.C. (2016). Hippocampal neuronal subtypes develop abnormal dendritic arbors in the presence of Fragile X astrocytes. *Neuroscience* 324, 202–217.
- Kang, M.H., Das, J., Gurunathan, S., Park, H.W., Song, H., Park, C., and Kim, J.H. (2017). The cytotoxic effects of dimethyl sulfoxide in mouse preimplantation embryos: a mechanistic study. *Theranostics* 7, 4735–4752.
- Kempermann, G., Song, H., and Gage, F.H. (2015). Neurogenesis in the Adult Hippocampus. *Cold Spring Harb. Perspect. Biol.* 7, a018812.
- Khandjian, E.W., Huot, M.E., Tremblay, S., Davidovic, L., Mazroui, R., and Barandon, B. (2004). Biochemical evidence for the association of fragile X mental retardation protein with brain polyribosomal ribonucleoparticles. *Proc. Natl. Acad. Sci. USA* 101, 13357–13362.
- Kim, M., Bellini, M., and Ceman, S. (2009). Fragile X mental retardation protein FMRP binds mRNAs in the nucleus. *Mol. Cell. Biol.* 29, 214–228.
- Kollipara, L., Buchkremer, S., Coraspe, J.A.G., Hathazi, D., Senderek, J., Weis, J., Zahedi, R.P., and Roos, A. (2017). In-depth phenotyping of lymphoblastoid cells suggests selective cellular vulnerability in Marinesco-Sjögren syndrome. *Oncotarget* 8, 68493–68516.
- Kořica, K., Lankoff, A., Banasik, A., Lisowska, H., Kuszewski, T., Góźdż, S., Koza, Z., and Wojcik, A. (2003). A cross-platform public domain PC image-analysis program for the comet assay. *Mutat. Res.* 534, 15–20.
- Kononenko, A.V., Ebersole, T., Vasquez, K.M., and Mirkin, S.M. (2018). Mechanisms of genetic instability caused by (CGG)<sub>n</sub> repeats in an experimental mammalian system. *Nat. Struct. Mol. Biol.* 25, 669–676.
- Korb, E., Herre, M., Zucker-Scharff, I., Gresack, J., Allis, C.D., and Darnell, R.B. (2017). Excess Translation of Epigenetic Regulators Contributes to Fragile X Syndrome and Is Alleviated by Brd4 Inhibition. *Cell* 170, 1209–1223.e20.
- Krawczun, M.S., Jenkins, E.C., and Brown, W.T. (1985). Analysis of the fragile-X chromosome: localization and detection of the fragile site in high resolution preparations. *Hum. Genet.* 69, 209–211.
- Kuwano, A., and Kajii, T. (1987). Synergistic effect of aphidicolin and ethanol on the induction of common fragile sites. *Hum. Genet.* 75, 75–78.
- Langmead, B., and Salzberg, S.L. (2012). Fast gapped-read alignment with Bowtie 2. *Nat. Methods* 9, 357–359.
- Le Beau, M.M., Rassool, F.V., Neilly, M.E., Espinosa, R., 3rd, Glover, T.W., Smith, D.I., and McKeithan, T.W. (1998). Replication of a common fragile site, FRA3B, occurs late in S phase and is delayed further upon induction: implications for the mechanism of fragile site induction. *Hum. Mol. Genet.* 7, 755–761.
- Le Tallec, B., Millot, G.A., Blin, M.E., Brison, O., Dutrillaux, B., and Debatisse, M. (2013). Common fragile site profiling in epithelial and erythroid cells reveals

- that most recurrent cancer deletions lie in fragile sites hosting large genes. *Cell Rep.* 4, 420–428.
- Li, H., Handsaker, B., Wysoker, A., Fennell, T., Ruan, J., Homer, N., Marth, G., Abecasis, G., and Durbin, R.; 1000 Genome Project Data Processing Subgroup (2009). The sequence alignment/map (SAM) format and SAMtools. *Bioinformatics* 25, 2078–2079.
- Li, Y., Stockton, M.E., Eisinger, B.E., Zhao, Y., Miller, J.L., Bhuiyan, I., Gao, Y., Wu, Z., Peng, J., and Zhao, X. (2018). Reducing histone acetylation rescues cognitive deficits in a mouse model of Fragile X syndrome. *Nat. Commun.* 9, 2494.
- Liu, S.X., Athar, M., Lippai, I., Waldren, C., and Hei, T.K. (2001). Induction of oxyradicals by arsenic: implication for mechanism of genotoxicity. *Proc. Natl. Acad. Sci. USA* 98, 1643–1648.
- Liu, W., Jiang, F., Bi, X., and Zhang, Y.Q. (2012). Drosophila FMRP participates in the DNA damage response by regulating G2/M cell cycle checkpoint and apoptosis. *Hum. Mol. Genet.* 21, 4655–4668.
- Matos, D.A., Zhang, J.M., Ouyang, J., Nguyen, H.D., Genois, M.M., and Zou, L. (2020). ATR Protects the Genome against R Loops through a MUS81-Trig-gered Feedback Loop. *Mol. Cell* 77, 514–527.e4.
- Murano, I., Kuwano, A., and Kajii, T. (1989). Fibroblast-specific common fragile sites induced by aphidicolin. *Hum. Genet.* 83, 45–48.
- Naim, V., Wilhelm, T., Debatissse, M., and Rosselli, F. (2013). ERCC1 and MUS81-EME1 promote sister chromatid separation by processing late replication intermediates at common fragile sites during mitosis. *Nat. Cell Biol.* 15, 1008–1015.
- Nakamoto, M., Nalavadi, V., Epstein, M.P., Narayanan, U., Bassell, G.J., and Warren, S.T. (2007). Fragile X mental retardation protein deficiency leads to excessive mGluR5-dependent internalization of AMPA receptors. *Proc. Natl. Acad. Sci. USA* 104, 15537–15542.
- Niere, F., Wilkerson, J.R., and Huber, K.M. (2012). Evidence for a fragile X mental retardation protein-mediated translational switch in metabotropic glutamate receptor-triggered Arc translation and long-term depression. *J. Neurosci.* 32, 5924–5936.
- Nishimura, Y., Martin, C.L., Vazquez-Lopez, A., Spence, S.J., Alvarez-Re-tuerto, A.I., Sigman, M., Steindler, C., Pellegrini, S., Schanen, N.C., Warren, S.T., and Geschwind, D.H. (2007). Genome-wide expression profiling of lymphoblastoid cell lines distinguishes different forms of autism and reveals shared pathways. *Hum. Mol. Genet.* 16, 1682–1698.
- Nott, A., and Tsai, L.H. (2013). The Top3 $\beta$  way to untangle RNA. *Nat. Neurosci.* 16, 1163–1164.
- Palakodeti, A., Han, Y., Jiang, Y., and Le Beau, M.M. (2004). The role of late/slow replication of the FRA16D in common fragile site induction. *Genes Chromosomes Cancer* 39, 71–76.
- Pansarasa, O., Bordoni, M., Drufuca, L., Diamanti, L., Sproviero, D., Trott, R., Bernuzzi, S., La Salvia, S., Gagliardi, S., Cerone, M., and Cereda, C. (2018). Lymphoblastoid cell lines as a model to understand amyotrophic lateral sclerosis disease mechanisms. *Dis. Model. Mech.* 11, dmm031625.
- Pérez-Pastén, R., Martínez-Galero, E., Garduño-Siciliano, L., Lara, I.C., and Cevallos, G.C. (2006). Effects of dimethylsulphoxide on mice arsenite-induced dysmorphogenesis in embryo culture and cytotoxicity in embryo cells. *Toxicol. Lett.* 161, 167–173.
- Pieretti, M., Zhang, F.P., Fu, Y.H., Warren, S.T., Oostra, B.A., Caskey, C.T., and Nelson, D.L. (1991). Absence of expression of the FMR-1 gene in fragile X syndrome. *Cell* 66, 817–822.
- Prado, F., and Aguilera, A. (2005). Impairment of replication fork progression mediates RNA polII transcription-associated recombination. *EMBO J.* 24, 1267–1276.
- Quinlan, A.R., and Hall, I.M. (2010). BEDTools: a flexible suite of utilities for comparing genomic features. *Bioinformatics* 26, 841–842.
- Ross-Innes, C.S., Stark, R., Teschendorff, A.E., Holmes, K.A., Ali, H.R., Dunning, M.J., Brown, G.D., Gojis, O., Ellis, I.O., Green, A.R., et al. (2012). Differential oestrogen receptor binding is associated with clinical outcome in breast cancer. *Nature* 481, 389–393.
- Sadowska-Bartosz, I., Pączka, A., Moloń, M., and Bartosz, G. (2013). Dimethyl sulfoxide induces oxidative stress in the yeast *Saccharomyces cerevisiae*. *FEMS Yeast Res.* 13, 820–830.
- Santoro, M.R., Bray, S.M., and Warren, S.T. (2012). Molecular mechanisms of fragile X syndrome: a twenty-year perspective. *Annu. Rev. Pathol.* 7, 219–245.
- Sanz, L.A., Hartono, S.R., Lim, Y.W., Steyaert, S., Rajpurkar, A., Ginno, P.A., Xu, X., and Chédin, F. (2016). Prevalent, Dynamic, and Conserved R-Loop Structures Associate with Specific Epigenomic Signatures in Mammals. *Mol. Cell* 63, 167–178.
- Savelyeva, L., and Brueckner, L.M. (2014). Molecular characterization of common fragile sites as a strategy to discover cancer susceptibility genes. *Cell. Mol. Life Sci.* 71, 4561–4575.
- Schindelin, J., Arganda-Carreras, I., Frise, E., Kaynig, V., Longair, M., Pietzsch, T., Preibisch, S., Rueden, C., Saalfeld, S., Schmid, B., et al. (2012). Fiji: an open-source platform for biological-image analysis. *Nat. Methods* 9, 676–682.
- Sethna, F., Moon, C., and Wang, H. (2014). From FMRP function to potential therapies for fragile X syndrome. *Neurochem. Res.* 39, 1016–1031.
- Siomi, H., Choi, M., Siomi, M.C., Nussbaum, R.L., and Dreyfuss, G. (1994). Essential role for KH domains in RNA binding: impaired RNA binding by a mutation in the KH domain of FMR1 that causes fragile X syndrome. *Cell* 77, 33–39.
- Verkerk, A.J., Pieretti, M., Sutcliffe, J.S., Fu, Y.H., Kuhl, D.P., Pizzuti, A., Reiner, O., Richards, S., Victoria, M.F., Zhang, F.P., et al. (1991). Identification of a gene (FMR-1) containing a CGG repeat coincident with a breakpoint cluster region exhibiting length variation in fragile X syndrome. *Cell* 65, 905–914.
- Voineagu, I., Surka, C.F., Shishkin, A.A., Krasilnikova, M.M., and Mirkin, S.M. (2009). Replisome stalling and stabilization at CGG repeats, which are responsible for chromosomal fragility. *Nat. Struct. Mol. Biol.* 16, 226–228.
- Wang, L., Darling, J., Zhang, J.S., Huang, H., Liu, W., and Smith, D.I. (1999). Allele-specific late replication and fragility of the most active common fragile site, FRA3B. *Hum. Mol. Genet.* 8, 431–437.
- Wang, J., Vasaikar, S., Shi, Z., Greer, M., and Zhang, B. (2017). WebGestalt 2017: a more comprehensive, powerful, flexible and interactive gene set enrichment analysis toolkit. *Nucleic Acids Res.* 45 (W1), W130–W137.
- Wongsurawat, T., Jenjaroenpun, P., Kwoh, C.K., and Kuznetsov, V. (2012). Quantitative model of R-loop forming structures reveals a novel level of RNA-DNA interactome complexity. *Nucleic Acids Res.* 40, e16.
- Xu, H., Rosales-Reynoso, M.A., Barros-Núñez, P., and Peprah, E. (2013). DNA repair/replication transcripts are down regulated in patients with fragile X syndrome. *BMC Res. Notes* 6, 90.
- Ying, S., Minocherhomji, S., Chan, K.L., Palmai-Pallag, T., Chu, W.K., Wass, T., Mankouri, H.W., Liu, Y., and Hickson, I.D. (2013). MUS81 promotes common fragile site expression. *Nat. Cell Biol.* 15, 1001–1007.
- Yu, S., and Lemos, B. (2016). A Portrait of Ribosomal DNA Contacts with Hi-C Reveals 5S and 45S rRNA Anchoring Points in the Folded Human Genome. *Genome Biol. Evol.* 8, 3545–3558.
- Zhang, Y., Liu, T., Meyer, C.A., Eeckhoute, J., Johnson, D.S., Bernstein, B.E., Nusbaum, C., Myers, R.M., Brown, M., Li, W., and Liu, X.S. (2008). Model-based analysis of ChIP-Seq (MACS). *Genome Biol.* 9, R137.
- Zhang, W., Cheng, Y., Li, Y., Chen, Z., Jin, P., and Chen, D. (2014). A feed-forward mechanism involving Drosophila fragile X mental retardation protein triggers a replication stress-induced DNA damage response. *Hum. Mol. Genet.* 23, 5188–5196.
- Zhu, L.J., Gazin, C., Lawson, N.D., Pagès, H., Lin, S.M., Lapointe, D.S., and Green, M.R. (2010). ChIPpeakAnno: a Bioconductor package to annotate ChIP-seq and ChIP-chip data. *BMC Bioinformatics* 11, 237.
- Zimonjic, D.B., Druck, T., Ohta, M., Kastury, K., Croce, C.M., Popescu, N.C., and Huebner, K. (1997). Positions of chromosome 3p14.2 fragile sites (FRA3B) within the FHIT gene. *Cancer Res.* 57, 1166–1170.
- Zorio, D.A., Jackson, C.M., Liu, Y., Rubel, E.W., and Wang, Y. (2017). Cellular distribution of the fragile X mental retardation protein in the mouse brain. *J. Comp. Neurol.* 525, 818–849.

## STAR★METHODS

### KEY RESOURCES TABLE

REAGENT or RESOURCE	SOURCE	IDENTIFIER
<b>Antibodies</b>		
Rabbit anti- $\gamma$ H2A.X (Ser139) conjugated to phycoerythrin	Cell Signaling Technology	Cat#5763S; RRID: AB_10706778
Rabbit anti- $\gamma$ H2A.X(Ser139)	Cell Signaling Technology	Cat#9718S; RRID: AB_2118009
Mouse S9.6 antibody	Kerafast	Cat#ENH001; RRID:AB_2687463
Chicken anti-Lamin A+C	Novus Biologicals	Cat#NBP2-25152; RRID: N/A
anti-nucleolin	Abcam	Cat#ab22758; RRID: AB_776878
Mouse anti-ATR	Santa Cruz Biotechnology	Cat#sc-516173; RRID: N/A
Rabbit anti-ATM	Abcam	Cat#ab32420; RRID: AB_725574
Mouse anti-Chk1	Santa Cruz Biotechnology	Cat#sc-8408; RRID: AB_627257
Mouse anti-RPA2	Abcam	Cat#ab2175; RRID: AB_302873
Mouse anti-H2A.X	Santa Cruz Biotechnology	Cat#sc-517336; RRID: N/A
Rabbit anti-phospho-ATR (Ser428)	Cell Signaling Technology	Cat#2853S; RRID: AB_2290281
Rabbit anti-phospho-ATM (Ser1981)	Abcam	Cat#ab81292; RRID: AB_1640207
Rabbit anti-phospho-Chk1 (Ser345)	Thermo Fisher Scientific	Cat#MA5-15145; RRID: AB_10979221
Rabbit anti-phospho-RPA2 (Thr21)	Abcam	Cat#ab109394; RRID: AB_10860648
Mouse anti-GAPDH	Santa Cruz Biotechnology	Cat#sc-47724; RRID: AB_627678
Mouse anti-FMRP	Biolegend	Cat#834601; RRID: AB_2564992
Mouse anti-FLAG-M2-Peroxidase (HRP)	Sigma-Aldrich	Cat#A8592-.2MG; RRID: AB_439702
Mouse anti-actin	MP Biomedical	Cat#691001; RRID: N/A
Donkey anti-Rabbit Secondary Antibody, Alexa fluor 488	Invitrogen	Cat#A-21206; RRID:AB_2535792
Donkey anti-Mouse Secondary Antibody, Alexa Fluor 568	Invitrogen	Cat#A10037; RRID:AB_2534013
Goat anti-Chicken Secondary Antibody, Alexa Fluor 647	Invitrogen	Cat#A-21449; RRID:AB_2535866
Goat anti-Rabbit Secondary Antibody, Alexa Fluor 647	Invitrogen	Cat#A-21244; RRID:AB_2535812
<b>Bacterial and Virus Strains</b>		
Turbo competent <i>E. coli</i> cells	NEB	Cat#C2984H
<b>Chemicals, Peptides, and Recombinant Proteins</b>		
TransIT-2020 transfection reagent	Mirus Bio	Cat#MIR 6003
poly-D-lysine	Sigma Aldrich	Cat#P6407
RNase H	NEB	Cat#M0297L
$\beta$ -Agarase I	NEB	Cat#M0392L
Aphidicolin	AG Scientific	Cat#A-1026-1mg
Propidium Iodide	Acros Organics	Cat#AC440300250
Prolong Diamond antifade mountant plus DAPI	Invitrogen	Cat#P36962
Halt protease and phosphatase inhibitor	Thermo Scientific	Cat#1861280
Biotin-14-dTAP	Invitrogen	Cat#19524016
Dynabeads M-270 Streptavidin	Invitrogen	Cat#65305
DMEM	GIBCO	Cat#11965-092
RPMI1640	Corning	Cat#15-040-CV
MEM	GIBCO	Cat#10370-021
BenchMark FBS heat inactivated	Gemini Bioproducts	Cat#100-106
FBS	Corning	Cat#350-010-CV
HEPES buffer	Corning	Cat#25-060-CI
Sodium pyruvate	Corning	Cat#25-000-CI
MEM nonessential amino acids	Corning	Cat#25-025-CI

(Continued on next page)

**Continued**

REAGENT or RESOURCE	SOURCE	IDENTIFIER
GlutaMAX	GIBCO	Cat#35050-061
Penicillin streptomycin solution	Corning	Cat#30-002-CI
KAPA HiFi HotStart Ready mix	Kapabiosystems/Roche	Cat#07958927001
AMPure XP beads	Beckman Coulter	Cat#A63880
Critical Commercial Assays		
CometAssay Kit	Trevigen	Cat#4250-050-K
Zombie Aqua Fixable Viability Kit	Biolegend	Cat#423101
End-It Kit	Epicenter/Lucigen	Cat#ER81050
A-tailing Kit	NEB	Cat#E6053L
Deposited Data		
Break-seq and DNA-seq sequencing data	This paper	GEO: GSE124403
GRCh37/hg19	UCSC human genome assembly	<a href="http://hgdownload.soe.ucsc.edu/goldenPath/hg19/bigZips/">http://hgdownload.soe.ucsc.edu/goldenPath/hg19/bigZips/</a>
Replication timing series in GM06990	Hansen et al., 2010	<a href="https://www.encodeproject.org/replication-timing-series/ENCSR595CLF/">https://www.encodeproject.org/replication-timing-series/ENCSR595CLF/</a>
APH_breakome	Crosetto et al., 2013	<a href="http://breakome.utmb.edu/supplementary_database/Downloads.html">http://breakome.utmb.edu/supplementary_database/Downloads.html</a>
NT2 and K562 cells_DRIP-seq	Sanz et al., 2016	GEO: GSE70189 (GSM1720615, GSM1720616, GSM1720617, GSM1720618, GSM1720619)
RLFS computationally predicted sequences	Wongsurawat et al., 2012	<a href="http://rlloop.bii.a-star.edu.sg/">http://rlloop.bii.a-star.edu.sg/</a>
Experimental Models: Cell Lines		
Human EBV transformed lymphoblastoid cell lines GM06990 (control)	Coriell Institute	GM06990; RRID:CVCL_9587
Human EBV transformed lymphoblastoid cell line: GM03200 (Fragile X)	Coriell Institute	GM03200; RRID:CVCL_AX76
Human fibroblast cell line: GM00357 (control)	Coriell Institute	GM00357; RRID:CVCL_6B36
Human fibroblast cell line: GM05848 (Fragile X)	Coriell Institute	GM05848; RRID:CVCL_AX83
Phoenix-AMPHO producer cells (ATCC)	ATCC	ATCC® CRL-3213; RRID:CVCL_H716
Experimental Models: Organisms/Strains		
<i>S. cerevisiae</i> : BY4741 ( <i>MATa his3Δ1 leu2Δ0 met15Δ ura3Δ0</i> )	Charlie Boone lab	N/A
<i>S. cerevisiae</i> : <i>rnh1Δ</i> ( <i>MATa rnh1Δ::KAN leu2Δ0 his3Δ1 met15Δ0 ura3Δ0</i> )	Charlie Boone lab	N/A
Oligonucleotides		
See Table S6 for the list of Oligonucleotides.		N/A
Recombinant DNA		
pcDNA3-EGFP	Addgene	Cat#13031, RRID:Addgene_13031
pMSCVpuro	Addgene	Cat#K1062-1, RRID: N/A
pFRT-TODestFLAGHAhFMRPiso1	Addgene	Cat#48690, RRID:Addgene_48690
pMSCVpuro-EGFP	This paper	N/A
pMSCVpuro-EGFP-FMRP	This paper	N/A
pARS-GLB-OUT	Prado and Aguilera, 2005	N/A
pARS-GLB-IN	Prado and Aguilera, 2005	N/A
pARS-GLB-OUT-Control-1	This paper	N/A
pARS-GLB-OUT-Control-2	This paper	N/A
pARS-GLB-IN-Control-1	This paper	N/A
pARS-GLB-IN-Control-2	This paper	N/A
pARS-GLB-OUT-RLFS1	This paper	N/A
pARS-GLB-OUT-RLFS2	This paper	N/A

(Continued on next page)

**Continued**

REAGENT or RESOURCE	SOURCE	IDENTIFIER
pARS-GLB-IN-RLFS1	This paper	N/A
pARS-GLB-IN-RLFS2	This paper	N/A
pFRT-TODestFLAGHAhFMRPiso1I304N	Addgene	Cat#48692, RRID:Addgene_48692
pRS313	ATCC	Cat#ATCC® 77142
pRS316	ATCC	Cat#ATCC® 77145
pRS313-CMV-FMRPiso1	This paper	N/A
pRS313-CMV-FMRPiso1I304N	This paper	N/A
pRS313-CMV-RNH1	This paper	N/A
pRS313-CMV-SHE2	This paper	N/A
Software and Algorithms		
DAVID Bioinformatics tools	Huang et al., 2009	<a href="https://david.ncifcrf.gov/">https://david.ncifcrf.gov/</a>
Bowtie 2	Langmead and Salzberg, 2012	<a href="http://bowtie-bio.sourceforge.net/bowtie2/index.shtml">http://bowtie-bio.sourceforge.net/bowtie2/index.shtml</a>
Picard MarkDuplicates	Broad Institute/ Github	<a href="http://broadinstitute.github.io/picard">http://broadinstitute.github.io/picard</a>
Samtools	Li et al., 2009	<a href="http://samtools.sourceforge.net/">http://samtools.sourceforge.net/</a>
BEDtools	Quinlan and Hall, 2010	<a href="https://bedtools.readthedocs.io/en/latest/">https://bedtools.readthedocs.io/en/latest/</a>
Preseq	Daley and Smith, 2013	<a href="https://github.com/smithlabcode/preseq">https://github.com/smithlabcode/preseq</a>
DiffBind	Ross-Innes et al., 2012	<a href="https://bioconductor.org/packages/release/bioc/html/DiffBind.html">https://bioconductor.org/packages/release/bioc/html/DiffBind.html</a>
ChIPpeakAnno R package (binOverFeature and annotatePeakInBatch functions)	Zhu et al., 2010	<a href="https://www.rdocumentation.org/packages/ChIPpeakAnno/versions/3.6.5/topics/binOverFeature">https://www.rdocumentation.org/packages/ChIPpeakAnno/versions/3.6.5/topics/binOverFeature</a> and <a href="https://www.rdocumentation.org/packages/ChIPpeakAnno/versions/3.6.5/topics/annotatePeakInBatch">https://www.rdocumentation.org/packages/ChIPpeakAnno/versions/3.6.5/topics/annotatePeakInBatch</a>
Model-based Analysis for ChIP-seq (MACS version 2.1.1)	Zhang et al., 2008	<a href="https://pypi.org/project/MACS2/">https://pypi.org/project/MACS2/</a>
Genomic Association Test	Heger et al., 2013	<a href="https://github.com/AndreasHeger/gat">https://github.com/AndreasHeger/gat</a>
WebGestalt	Wang et al., 2017	<a href="http://webgestalt.org">http://webgestalt.org</a>
Fiji	Schindelin et al., 2012	<a href="https://fiji.sc/">https://fiji.sc/</a>
Graphpad Prism		<a href="https://www.graphpad.com/scientific-software/prism/">https://www.graphpad.com/scientific-software/prism/</a>
OpenComet v1.3.1	Gyori et al., 2014	<a href="https://www.cometbio.org">https://www.cometbio.org</a>
Kaleidagraph	Hoover, 2000	<a href="https://www.synergy.com">https://www.synergy.com</a>
Flowjo	Ashland, OR: Becton, Dickinson and Company	<a href="https://www.flowjo.com">https://www.flowjo.com</a>
SeqMonk v1.43.0	Babraham Bioinformatics	<a href="https://www.bioinformatics.babraham.ac.uk/">https://www.bioinformatics.babraham.ac.uk/</a>

**RESOURCE AVAILABILITY**

**Lead Contact**

Further information and requests for resources and reagents should be directed to and will be fulfilled by the Lead Contact, Wenyi Feng ([fengw@upstate.edu](mailto:fengw@upstate.edu)).

**Materials Availability**

Plasmids generated in this study will be made available upon request following publication.

**Data and Code Availability**

All primary sequencing data and processed data described in this manuscript have been deposited in the NCBI Gene Expression Omnibus (GEO; <http://www.ncbi.nlm.nih.gov/geo/>) under the accession number GEO: GSE124403.

## EXPERIMENTAL MODEL AND SUBJECT DETAILS

### Cell line growth and culture conditions

Human EBV transformed lymphoblastoid cell lines, GM06990 (control) and GM03200 (Fragile X), and fibroblast cell lines, GM00357 (control) and GM05848 (Fragile X), were purchased from Corielle institute. Lymphoblastoids were grown in RPMI1640 (Corning), supplemented with GlutaMAX (GIBCO), 15% heat-inactivated FBS (Fetal Bovine Serum, Benchmark), 100 IU/mL penicillin and 100 µg/mL streptomycin (Corning) at 37°C with 5% CO<sub>2</sub>. Fibroblast cells were cultured in MEM culture media with 15% FBS (Corning), 1X GlutaMAX, 100 IU/mL penicillin and 100 µg/mL streptomycin. Cell lines were verified for presence or absence of FMRP and expansion of the *FMR1* 5'UTR using western blot and Southern blot respectively. See Figures 1A and S1A for results. Phoenix-AMPHO producer cells (ATCC) were grown in DMEM medium (GIBCO) supplemented with 10% FBS, 1X GlutaMAX, 100 IU/mL penicillin and 100 µg/mL streptomycin, 1mM sodium pyruvate (Corning), 10mM HEPES buffer (Corning) and 1X MEM non-essential amino acids (Corning).

### Yeast strains

Yeast strains used in this study were BY4741 (*MATa his3Δ1 leu2Δ0 ura3Δ0 met15Δ1*) and its isogenic derivative *rnh1Δ* (*MATa ura3Δ0 leu2Δ0 his3Δ1 met15Δ0 rnh1Δ::KAN*, EUROSCARF collection (Entian et al., 1999)). Yeast cells were either grown in YEPD or synthetic complete (SC) media with specific amino acids omitted as indicated in ‘Recombination Frequency Assay’ below. All yeast strains were grown at 30°C with horizontal shaking for liquid cultures.

## METHOD DETAILS

### Cell line drug treatment conditions

Cells were treated at a density of 0.4–0.5x10<sup>6</sup> cells/ml or 30%–40% confluence for lymphoblastoids and fibroblasts, respectively, with APH (A. G. Scientific) at the indicated concentrations, solvent (DMSO, 0.02%, same as the concentration in the APH-treated samples) only, or nothing, for 24 h before harvest.

### Cloning

EGFP was PCR amplified from pcDNA3-EGFP (Addgene #13031) using forward primer, pcDNA3\_RMEGFP\_JL\_FWD2, and reverse primer, pcDNA3\_RMEGFP\_JL\_REV2, and cloned into pMSCVpuro (Addgene K1062-1) at the Hpal site to create pMSCVpuro-EGFP. Full length *FMR1* was PCR amplified from pFRT-TODestFLAGHAhFMRPiso1 (Addgene #48690) using forward primer, pFRT\_RMFMRP\_JL\_FWD2 and reverse primer, pFRT\_RMFMRP\_JL\_REV2, and cloned into pMSCVpuro-EGFP at EcoRI site, creating pMSCVpuro-EGFP-FMRP.

### Lentiviral-assisted cell transfection

pMSCVpuro-EGFP-FMRP and pMSCVpuro-EGFP constructs were packaged into retrovirus using Phoenix-AMPHO producer cells (ATCC) following the manufacturer’s protocol. Briefly, Phoenix cells were grown to 30%–40% confluence in a 100-mm plate and were transfected with 20 µg plasmid DNA using 60 µl of TransIT-2020 transfection reagent (Mirus Bio), followed by incubation at 37°C for 48 h with a medium change at 24 h. At 48 h, the supernatant containing virus (T1) was collected, passed through a 0.45-µm filter, and used immediately for infection, while the remaining cells was used for second round of virus collection after the addition of 8 mL fresh DMEM. A second production of virus (T2) was collected after 24 h, processed as described above and used for a second round of infection. GM05848 (FX) cells were transduced for two rounds with retrovirus produced above, pooled and subjected to 2 µg/ml puromycin selection for 3 days. Cells were passaged after reaching confluence and maintained in DMEM containing 0.25 µg/ml puromycin. FMRP expression was confirmed with western blot.

### Flow cytometry for cell cycle analysis

Approximately 1.5–2x10<sup>6</sup> cells from the Break-seq experiments were harvested for flow cytometry. Cells suspended in 1 mL of PBS were slowly added to chilled absolute ethanol and stored in –20°C. Fixed cells were pelleted at 250xg for 15 m at room temperature and then rehydrated with 5 mL PBS for 15 m. Cells were again pelleted and resuspended at 0.5x10<sup>6</sup> cells/ml in propidium iodide solution (40 µg/ml propidium iodide, 100 µg/ml RNase A in PBS) and incubated for 20 m at 37°C. Cells were passed through filter-tipped flow tubes (BD Falcon) using a luer-lock syringe and analyzed using Becton Dickinson Fortessa Cell Analyzer (BD Biosciences). Data were analyzed by FlowJo.

### Flow cytometry for quantification of cells stained for γH2A.X

Approximately 3x10<sup>6</sup> lymphoblastoids were treated with APH, DMSO or nothing. For compensation control, an additional 3x10<sup>6</sup> cells were subjected to 2 flashes of UV irradiation at 20 µJ/cm<sup>2</sup> and allowed to recover for 4 h before harvest. Cells were treated with 1:500 diluted Zombie Aqua (Violet, Biolegend) to stain dead cells, followed by a wash in FACS buffer (2% FBS in PBS). Cells were then fixed in 500 µL of 4% paraformaldehyde, permeabilized by 500 µL methanol, and stained with 100 µL of a 1:50 dilution of anti-γH2A.X conjugated to phycoerythrin (Cell signaling #5763S) in dilution buffer (0.5% BSA in 1x PBS) for 1 h. Cells were then centrifuged and

washed in dilution buffer followed by 1x PBS. Cells were resuspended in FACS buffer and filtered through filter-topped flow tubes (BD falcon) using a luer-lock syringe. Samples were analyzed using Becton Dickinson Fortessa Cell Analyzer (BD Biosciences) and data analyzed by FlowJo. Live and  $\gamma$ -H2A.X-positive cells were gated by Zombie Aqua dye (staining for dead cells) and  $\gamma$ -H2A.X signals from untreated NM cells. The same gate was applied to all other samples for quantification of percentage of cells with  $\gamma$ -H2A.X signals greater than those gated cells (solid red boxes in Figure 1). Ten thousand cells were analyzed in each of three independent experiments. Percentage of cells with DNA damage were calculated based on the number of cells above the baseline FI and total live cells.

### Immunocytochemistry and microscopy

*For lymphoblastoid cells:* Approximately  $3 \times 10^6$  cells having undergone drug treatment described above were washed twice in PBS before fixing with 500  $\mu$ L of methanol or 4% paraformaldehyde in microfuge tubes. *For fibroblasts:* Approximately  $1 \times 10^5$  cells were plated on poly-D-lysine (Sigma Aldrich)-coated coverslips and cultured for 72 h, followed by drug treatment for 24 h. *For both lymphoblastoid cells and fibroblasts:* Cells were washed with 500  $\mu$ L PBS twice, fixed with 500  $\mu$ L 2%-4% paraformaldehyde for 20 m at room temperature followed by gentle washing with PBS three times. Cells were then blocked with 500  $\mu$ L PBSAT (1% BSA, 0.5% Triton X in PBS) for 1 h, followed by incubation with 100  $\mu$ L of primary antibody solution for 1 h or overnight, washed with PBSAT, and incubation with 100  $\mu$ L secondary antibody for 1 h. For experiments with RNase H treatment, cells were first permeabilized with PBSAT for 20 m before incubation with 15 U RNase H (NEB M0297L) in 500  $\mu$ L reaction buffer per sample, with control cells incubated in 500  $\mu$ L of PBS per sample, at 37°C for 3 h. Cells were then blocked with PBSAT and incubated with antibodies as described above. Cells were then washed with PBSAT, followed by PBS, and mounted onto microscope slides in mounting media (Prolong Diamond antifade plus DAPI, Invitrogen) and allowed to solidify for 24 h before imaging on Leica STP 800 wide-field fluorescence microscope (for lymphoblasts) or Leica SP8 confocal (for fibroblasts). Antibodies used for immunostaining include the following: primary antibodies (anti- $\gamma$ H2A.X, Cell Signaling #9817S, 1:400; S9.6, Kerafast #ENH001, 1:250; anti-Lamin A&C, Novus Biologicals #NBP2-25152, 1:500; and anti-nucleolin, Abcam #22758, 1:1000) and secondary antibodies (Alexa fluor 488, 568, and 647 [anti-chicken or anti-rabbit], Invitrogen #A21206, A10037, A21449, A21244 respectively, 1:400).

To quantify  $\gamma$ H2A.X staining signals maximum projection of 3D image stacks acquired from 2D imaging planes with a step size of 0.2 micron along the z axis was performed using the MetaMorph software (Molecular Devices). Image stacks were deconvolved using the AutoQuant software. In Fiji, DAPI was used to create region of interest (ROI) of nuclei in  $\gamma$ H2A.X channel for individual cells. Maximum intensity projections adjusted for background in Fiji were used to quantify  $\gamma$ H2A.X intensities in ROI. At least 28 nuclei per sample per experiment in three independent experiments were analyzed. To determine R-loop signals in the nucleus, 2D single plane images from two biological replicate experiments were acquired and analyzed. Lamin or DAPI staining was used to define the nuclear periphery, which was overlaid with S9.6 channel to measure integrated density in Fiji. Representative images adjusted for background and contrast are shown. Statistical analysis was done using GraphPad Prism 7 and values were plotted in Kaleidograph.

### Single cell gel electrophoresis assay

Neutral comet assay was performed using the TREVIGEN reagent kit (cat#4250-050-K) according to the manufacturer's instructions. Comet images were analyzed using the CaspLab software (Kočka et al., 2003).

### Break-seq library construction

Lymphoblastoids GM03200 and GM06990 were used for Break-seq analysis. Three independent experiments were performed, wherein Set A and B were technical replicates from the same experiment and Set D and E were biological replicates. Break-seq procedures were as described previously with modifications (Hoffman et al., 2015).  $5 \times 10^6$  cells were embedded into 0.5% Incert low-melting point agarose in PBS and cast into plugs. The agarose plugs were then incubated at 50°C overnight in 6 mL of lysis buffer (0.5 M EDTA, 1% Sarkosyl, 200  $\mu$ g/ml Proteinase K). The DNA in the agarose plugs was then end-labeled in-gel using the End-It Kit (Epicenter) with biotinylated dNTP mix (1 mM dTTP, dCTP, dGTP, 0.84 mM dATP, 0.16 mM Biotin-14-dATP). Plugs were then treated with  $\beta$ -Agarase (NEB) to digest agarose and release DNA. DNA sample was then sonicated using a Covaris M220 using the snap-cap DNA 300 bp shearing protocol. DNA was then processed using a PCR Cleanup Kit (QIAGEN) and run on agarose gel to verify the fragmentation pattern of DNA and quantified on a Nanodrop. 10-11  $\mu$ g of DNA was then end repaired (Epicenter) and purified by the PCR Cleanup Kit (QIAGEN). The DNA was then A-tailed by A-tail Kit (NEB) or Klenow exo- (NEB E6054A) and purified by PCR Clean-up Kit (QIAGEN), followed by quantification on a Nanodrop. M270 Dynabeads (Life Technologies) were used to purify biotinylated DNA. The amount of DNA bound to beads was calculated by measuring the quantity of DNA in the flow through. DNA-bound beads were then resuspended in ligation mix containing Illumina adaptors (50  $\mu$ M adaptor-1, 50  $\mu$ M adaptor-2, 1x T4 ligase buffer, 3  $\mu$ L T4 DNA ligase) and incubated overnight at room temperature on a roller. 400 ng of DNA bound to beads was used for PCR amplification using KAPA Hotstart Ready Mix (KAPA). Each sample was given a specific index primer for multiplexing. PCR product was then run on agarose gel to verify amplification and quantity. AMPure beads (Agencourt) were used to remove free adaptors and the final product was analyzed on agarose gel. Break-seq libraries were sequenced on Illumina Hi-Seq 2500 with 100 or 150 bp paired-end reads, followed by Break-seq data analysis. Adapter sequences and index primer sequences were previously described (Hoffman et al., 2015).

### Western blot

For protein expression in human cell lines, whole cell extracts were prepared by lysing cells in RIPA buffer (50mM Tris HCl pH 7.4 / 150mM NaCl / 0.5% sodium deoxycholate / 0.1% sodium dodecyl sulfate/ 1% NP-40) containing Halt protease and phosphatase inhibitor cocktail (Thermo Scientific) and approximately 20 µg of proteins were analyzed by 4%–15% gradient TGX Precast polyacrylamide gel (Bio-Rad), transferred onto a nitrocellulose membrane and probed for specific proteins. The following antibodies were used: anti-ATR (Santa Cruz Biotechnology #sc-516173, 1:250), anti-ATM (abcam #ab32420, 1:250), anti-Chk1 (Santa Cruz Biotechnology #sc-8408, 1:100), anti-RPA2 (abcam #2175, 1:200), anti-H2A.X (Santa Cruz Biotechnology #sc-517336, 1:1000), anti-phospho-ATM (Ser1981) (abcam #ab81292, 1:500), anti-phospho-ATR (Ser428) (Cell signaling technology #2853S, 1:500), anti-phospho-Chk1 (Ser345) (ThermoFisher Scientific #MA5-15145, 1:50), anti-phospho-RPA2 (Thr21) (abcam #109394, 1:1000), anti-phospho-H2A.X (Ser139) (Cell signaling technology #9817S, 1:250), anti-GAPDH (Santa Cruz Biotechnology #sc-47724, 1:1000) and anti-FMRP (Biologen #834601, 1:1000).

For yeast whole cell extracts, a single colony was inoculated in 10 mL SC-HIS-URA and grown overnight. Cells were centrifuged at 3000 rpm for 5 m, frozen and stored at –80°C until further use. Frozen cell pellets were thawed in 250 µL TBS [50 mM Tris pH 7.5 / 100 mM NaCl / Halt protease inhibitor cocktail (Thermo Scientific)]. Cell suspension was vortexed at 4°C for 15 m after the addition of 200 µL sterile glass beads, followed by centrifugation at 13500 rpm at 4°C for 10 m. The supernatant was retained and protein concentration was determined by Bradford assay (BioRad). Approximately 25 µg of proteins was analyzed on 10% SDS-PAGE followed by western blots using monoclonal anti-FLAG-M2-Peroxidase (HRP) (Sigma Aldrich, 1:2000) and anti-actin (MP Biochemical, 1:4000).

### Yeast strains and plasmids

Yeast centromeric plasmids pARS-GLB-OUT (OUT) and pARS-GLB-IN (IN) containing GAL-OUT/IN recombination constructs were provided by and described previously ([Prado and Aguilera, 2005](#)). Specifically, these plasmids were designed with the *leu2Δ3':leu2Δ5'* direct-repeat recombination system under the *GAL1* promoter. The plasmid also contains *ARSH4*, *URA3*, *CEN6* and the 83 bp (C-A1-3)<sub>n</sub> telomeric sequences from pRS304 lacking the *EcoRI* site at the polylinker. Human gene sequences for recombination assay (see below) were cloned between the direct-repeat recombination system (*leu2Δ3':human gene sequence:leu2Δ5'*) using *BglII*. The following primers containing *BglII* site in the forward and *BamHI* site in the reverse were used for the described sequences: a) control-1\_F and control-1\_R; b) control-2\_F and control-2\_R; c) RLFS-1\_F and RLFS-1\_R; d) RLFS-2\_F and RLFS-2\_R.

The above sequences were PCR amplified from human genomic DNA. Sequences were inserted in two orientations due to compatibility of ends generated by *BglII* and *BamHI* and both the orientations were used to measure recombination frequencies for all sequences. The sequences were inserted in both the IN and the OUT constructs. pFRT-TODestFLAGHAhFMRPiso1 plasmid (Addgene) was used to subclone an *SpeI/BclI*-digested CMV-FMRPiso1 fragment into pRS316 at the *XbaI* and *BamHI* cloning sites. The resulting construct, pRS316-CMV-FMRPiso1, was then digested with *NotI* and *EcoRI* to obtain the CMV-FMRPiso1 fragment. The fragment was subcloned into pRS313 digested with *NotI* and *EcoRI* producing the final construct pRS313-CMV-FMRPiso1. pRS313-CMV-FMRPiso1I304N was generated using the same procedure from the pFRT-TODestFLAGHAhFMRPiso1I304N plasmid (Addgene).

### Recombination frequency assay

The IN and OUT plasmids were first transformed in BY4741 or *rnh1Δ* and selected in SC without uracil in 2% glucose. The fluctuation assay was performed as previously described with modifications ([Prado and Aguilera, 2005](#)). Briefly, selected transformants were streaked onto SC-URA+2% Glucose and SC-URA+3% Galactose. Plates were incubated for 4 days at 30°C to suppress or induce transcription through the *GAL1* promoter respectively. Six single colonies for every sample were re-suspended in 1 mL –N media (1.61 g/l YNB without (NH4)<sub>2</sub>SO<sub>4</sub> or amino acids, 94 mM succinic acid and 167 mM NaOH) and sonicated. Serial dilutions were prepared for each of the six colonies per sample: 1:15, 1:150 and 1:1500 in a 96-well plate. 100 µL of diluted samples were plated in SC-URA+3% Galactose for calculation of totals. For calculation of recombinants; 100 µL from undiluted was plated onto SC-LEU-URA+3% Galactose. Plates were incubated for 3 days at 30°C, and colonies were counted to calculate recombination frequency as follows:

$$\text{no. of recombinant colonies} / (\text{total no. of cells plated} * \text{dilution factor}) * 10^4$$

Recombination frequency was calculated for each of the six colonies per sample and the median value was used as the recombination frequency of a sample. Three independent experiments were conducted for each construct and treatment (glucose and galactose) and standard deviations were calculated for graphical representation and to estimate error.

For experiments with FMRP expression the IN and OUT plasmids with or without RLFS were co-transformed with pRS313-CMV-FMRPiso1, pRS313-CMV-FMRPiso1I304N or pRS313 into BY4741 and selected in SC-URA-HIS+2% glucose. Recombination frequency assay was conducted as described above with the totals plated in SC-URA-HIS+3% galactose and the recombinants were plated in SC-LEU-URA-HIS+3% galactose.

**Gene ontology analysis and identification of pathways that are potentially altered by treatment**

Gene ontology analyses were performed via DAVID Bioinformatics tools (<https://david.ncifcrf.gov>), DiffBind, or WebGestalt (<http://webgestalt.org>).

**QUANTIFICATION AND STATISTICAL ANALYSIS****Break-seq DSB peak identification**

Raw sequence reads were obtained from Illumina Hi-seq 2500 and then aligned to the UCSC human genome assembly, GRCh37/hg19 (<http://hgdownload.soe.ucsc.edu/goldenPath/hg19/bigZips/>), using Bowtie 2 (<http://bowtie-bio.sourceforge.net/bowtie2/index.shtml>) in the “–local” mode. The PCR duplicate reads were removed using Picard MarkDuplicates (<http://broadinstitute.github.io/picard>). The non-redundant mapped sequence reads were sorted and then converted to BAM files using SAMtools (Li et al., 2009) (<http://samtools.sourceforge.net>) and subjected to subsequent processing with Model-based Analysis for ChIP-seq (MACS version 2.1.1, <https://pypi.org/project/MACS2/2.1.1.20160309/>) using two-sample analysis between break-seq samples (treatment) and whole genome sequencing data (control) using the *callpeak* function in MACS2 with a p value < 1e-5. For identification of *PacI*-digested breaks, DSB peaks with perfect match to *PacI* motif (TTAATTAA) were mapped onto the hg19 reference genome with Bowtie. *IntersectBED* function from BEDtools (Quinlan and Hall, 2010) was then used to find overlap between *PacI* motif sites and peaks identified through MACS2. These overlapping peaks were considered *PacI* sites found in the Break-seq sample.

**Random permutation tests for identification of *PacI* sites**

The *shuffleBed* function in BEDtools was used to randomly permute the genomic locations of DSBs identified as *PacI* sites with default parameters to generate random genomic locations as a null distribution, preserving the size of DSBs and number of DSBs per chromosome. The fraction of sequences containing *PacI* motif was calculated. One thousand iterations of this process were performed. The distribution of the *PacI*-positive fractions was then compared to that from the experimental dataset and One Sample Student's t test was performed.

**Break-seq library complexity calculation and identification of consensus DSB peaks in replicate experiments**

All biological replicates for each sample (strain/treatment combination) were pooled for assessment of library complexity by preseq (Daley and Smith, 2013). All 23 Break-seq peak files were analyzed in DiffBind (Ross-Ihnes et al., 2012) for consensus DSB peak identification. Consensus DSB peaks were defined as those that appear in at least two replicate experiments, regardless of the total number of replicates, for each sample (cell line/treatment). Aphidicolin-treated samples (0.03 µM and 0.3 µM) were combined to form a composite APH-treated sample, for both NM and FX cells, and consensus DSB peaks were then extracted similarly as described.

**Correlation between DSBs and other genomic features**

The association between DSBs and other genomic features including RLFSs and DRIP-seq signals was determined using the *bedtools annotate* function. Multiple datasets of DRIP-seq were concatenated (*cat GSE70189\_NT2\_DRIPc\_peaks GSM1720615\_NT2\_DRIP\_1\_peaks GSM1720616\_NT2\_DRIP\_2\_peaks GSM1720617\_NT2\_DRIP\_RNaseA\_peaks GSM1720618\_NT2\_DRIP\_RNaseH\_peaks GSM1720619\_K562\_DRIP\_peaks.clip > composite.DRIP*), sorted (*sort -k1,1 -k2,2n composite.DRIP > composite.DRIP.sorted*) and then merged into a composite dataset using the *bedtools merge* function (*bedtools merge -i composite.DRIP.sorted > composite.DRIP.sorted.merged*). The significance of the association or p value was calculated using the fisher exact test (*fisher*) in BEDtools (<https://bedtools.readthedocs.io/en/latest/content/tools/fisher.html>). Calculation of DSB coverage over RLFS and annotation of genes associated with DSBs were performed with the *binOverFeature* and *annotatePeakInBatch* functions from the ChIPpeakAnno R package, respectively (Zhu et al., 2010).

**Calculation of replication timing for DSB regions**

Replication timing data were derived from Repli-seq data of lymphoblastoid GM06990 cells (accession: ENCSR595CLF) publicly available from ENCODE (<https://www.encodeproject.org/replication-timing-series/ENCSR595CLF/>). An S50 (0 < S50 < 1) value, defined as the fraction of the S phase at which 50% of the DNA is replicated (50% of the cumulative enrichment), was computed for any 50-kb segment of the genome (Hansen et al., 2010). The cumulative enrichment was calculated for each sliding window of 50 kb at a 1-kb step size by linear interpolation of enrichment values in 6 evenly divided temporal windows of the S phase, as previously described (Chen et al., 2010). If a given 50-kb segment was not significantly enriched in any window in the S phase, no S50 value was attributed (S50 = NA). Approximately 5% of the genome fell in this category. The DSB regions were then assigned the same S50 values as that of the 50-kb segment in which they reside. For FX cells DSBs on the Y chromosome were excluded from further analysis due to the lack of replication timing data in the reference genome of GM06990. Finally, the DSBs with assigned replication timing values were further parsed into early (S50 < 0.5) and late (S50 > 0.5) replicating domains. The resulting distribution of DSBs in the early and late replicating domains was subjected to a Genomic Association Test (GAT) to determine if the DSBs were enriched in either of the two domains through 1000 randomized simulation (Heger et al., 2013).

**Genomic association tests for correlation between DSBs and CFS cores and the “APH.breakome.”**

The DSB regions with assigned replication timing indices (early versus late, see above) were compared to previously published finely mapped CFS core sequences ([Le Tallec et al., 2013](#); [Savelyeva and Brueckner, 2014](#)) and the “APH.breakome” ([Crossetto et al., 2013](#)), using the Genomic Association Tester (GAT) software ([Heger et al., 2013](#)). In all tests the DSBs were set as *segments* and the other datasets as *annotation*, with the genomic regions previously assigned with S50 values as *workspace* (i.e., excluding those regions with S50 value of “NA”) and default parameter for sampling rounds (–num-samples = 1000).

**Statistical analysis**

Two-way ANOVA test followed by Tukey’s multiple testing for all pairwise comparisons was performed for all experiments unless otherwise noted. Annotation for P values in figure legends regardless of statistical test type are: \*, p < 0.05; \*\*, p < 0.01; \*\*\*, p < 0.001; \*\*\*\*, p < 0.0001. Error bars denote standard deviation unless otherwise noted.

**Supplemental Information**

**Replication Stress Induces Global Chromosome  
Breakage in the Fragile X Genome**

**Arijita Chakraborty, Piroon Jenjaroenpun, Jing Li, Sami El Hilali, Andrew McCulley, Brian Haarer, Elizabeth A. Hoffman, Aimee Belak, Audrey Thorland, Heidi Hehnly, Carl Schildkraut, Chun-long Chen, Vladimir A. Kuznetsov, and Wenyi Feng**

## Supplemental Figure S1

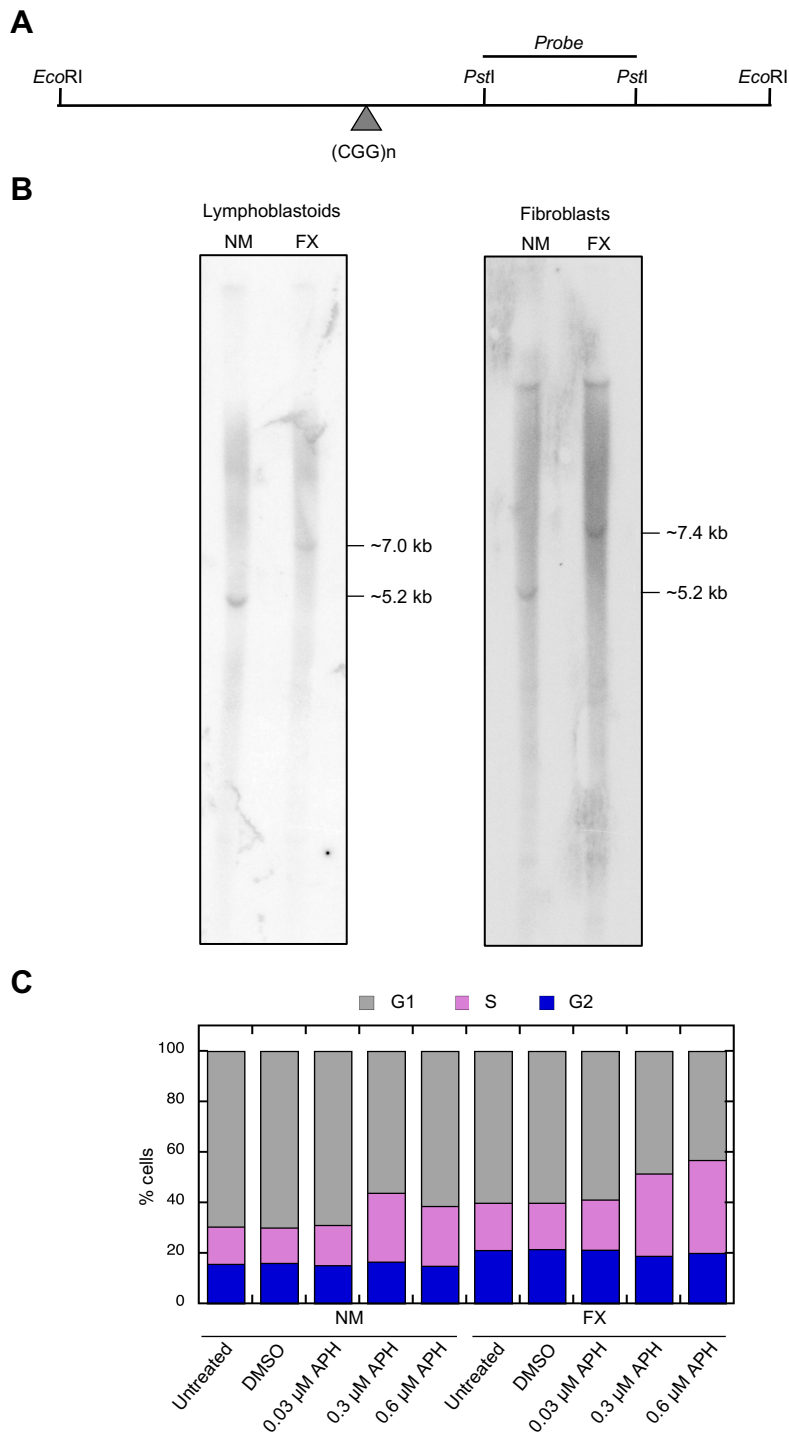


**Figure S1. Related to Figure 1A. Validation of CGG repeat expansion at *FMR1* locus and the absence of FMRP expression in the Fragile X cell lines used in this study. (A)** The restriction map of the 5.2 kb *EcoRI* fragment in the *FMR1* locus and probe position used for Southern blots are shown. The probe was synthesized by PCR amplification from genomic DNA isolated from GM06990 using the following primers: FMR1-F, 5'-TGGCTTCTCTTTCCGGTCT-3'; FMR1-R, 5'-GGGTTACCTTTGCCTCCTT -3'. **(B)** Southern blots of *EcoRI*-digested genomic DNA from the indicated cell lines. A band corresponding to 5.2 kb (containing 30-50 CGG repeats) was seen in the normal cell lines. In contrast, two bands corresponding to ~7.0 kb and ~7.4 kb were identified in the FX lymphoblastoid and fibroblast lines, which correspond to ~590 and 730 CGG repeat expansion, respectively. **(C)** Cell cycle distribution analyzed by flow cytometry. Three independent experiments were conducted, and one representative experiment is shown.

## Supplemental Figure S2

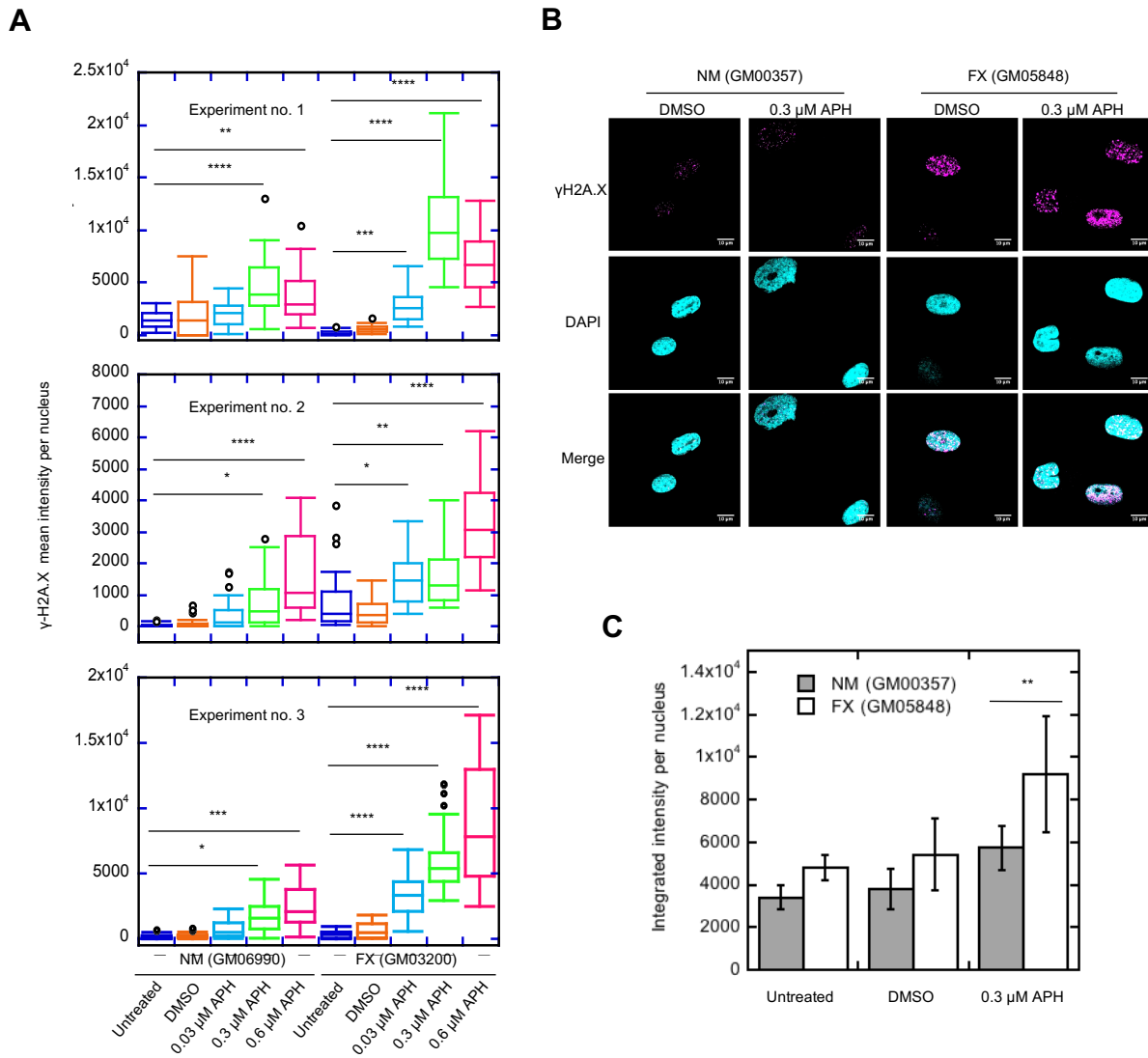


**Figure S2. Related to Figure 1B. Lymphoblastoid cells and fibroblasts from FX have increased DNA damage.** (A) Box plots for  $\gamma$ -H2A.X immunofluorescence staining of lymphoblastoid cells under the indicated conditions from **Figure 1B**. Plotted are mean intensity values of fluorescence per nucleus in three independent experiments ( $n \geq 28$  nuclei counted for each experiment). One-way ANOVA test followed by Tukey's multiple comparison test were performed. (B&C) Fibroblast cell line from a FX individual shows increased DNA damage compared to a sex and age matched control fibroblast cell line. Two independent experiments were performed, and one representative experiment is shown here. At least 41 nuclei per sample were analyzed in each experiment. Representative images for  $\gamma$ H2A.X staining in FX and NM cells under the indicated treatment (B) and quantification of  $\gamma$ H2A.X signals per nucleus (C) are shown. Error bars indicate standard deviation. Two-way ANOVA test followed by Sidak's multiple testing was performed. \* $p < 0.05$ , \*\* $p < 0.01$ , \*\*\* $p < 0.001$  and \*\*\*\* $p < 0.0001$ . Scale bar, 10  $\mu$ m.

## Supplemental Figure S3

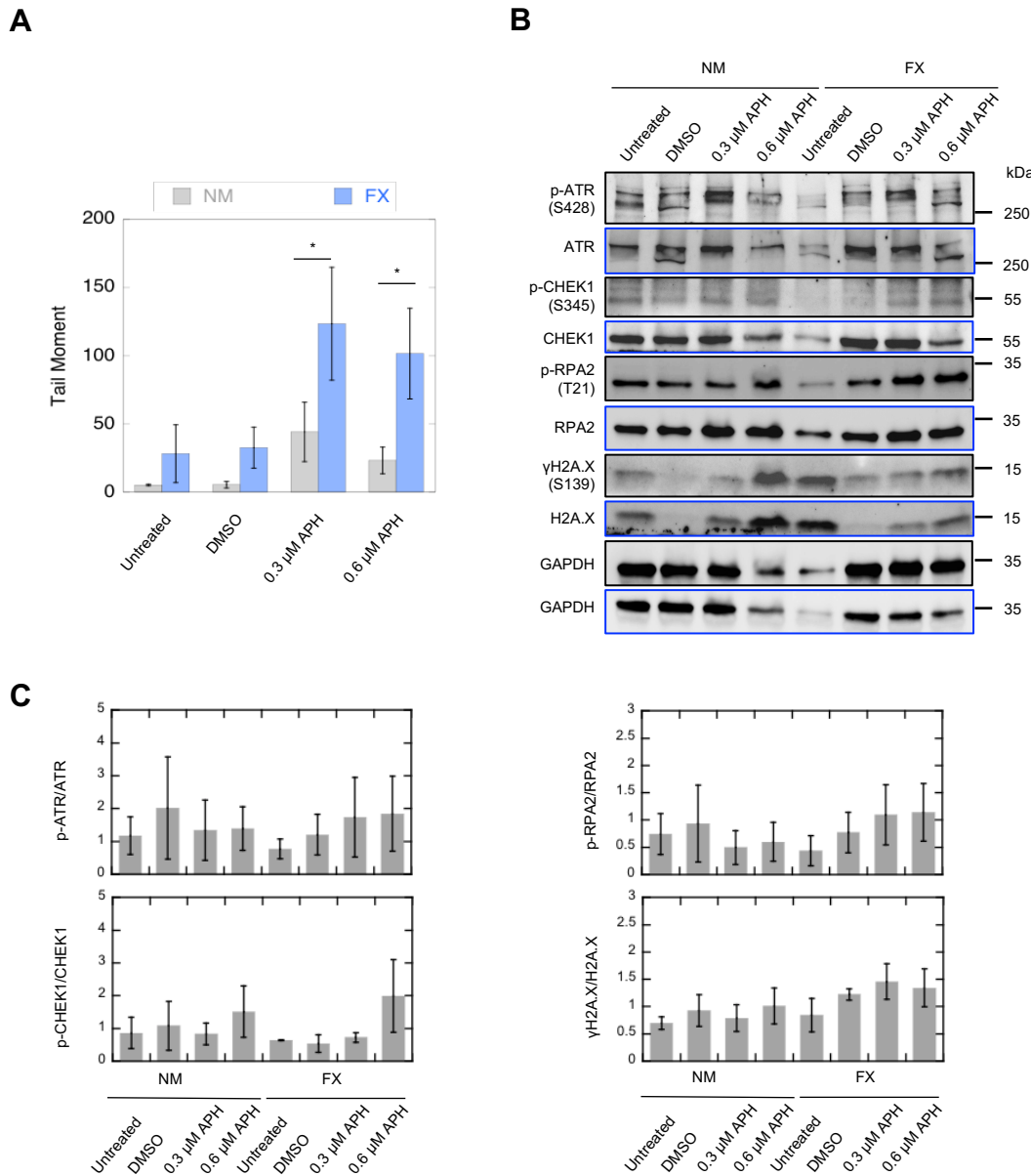


**Figure S3. Related to Figures 1E&F. DNA damage is elevated and DDR is not impaired in FX cells.** (A) DSB formation measured by neutral Comet assay. Three independent experiments were performed ( $n>50$  in each) and all trended similarly. A representative experiment is shown for Tail Moment measurement. One-way ANOVA followed by Sidak's multiple testing was performed. Error bars denote standard errors of mean and  $*p<0.05$ . (B) Whole cell lysates from NM and FX lymphoblastoid cells western blotted for proteins in the DDR pathway. Blots probed with antibodies against phospho(p)-proteins and total proteins are shown in black and blue bordered panels, respectively. Both sets of blots were controlled for loading using GAPDH. (C) Quantification of phosphorylation of DDR proteins in (A). Error bars indicate standard error of mean.

## Supplemental Figure S4

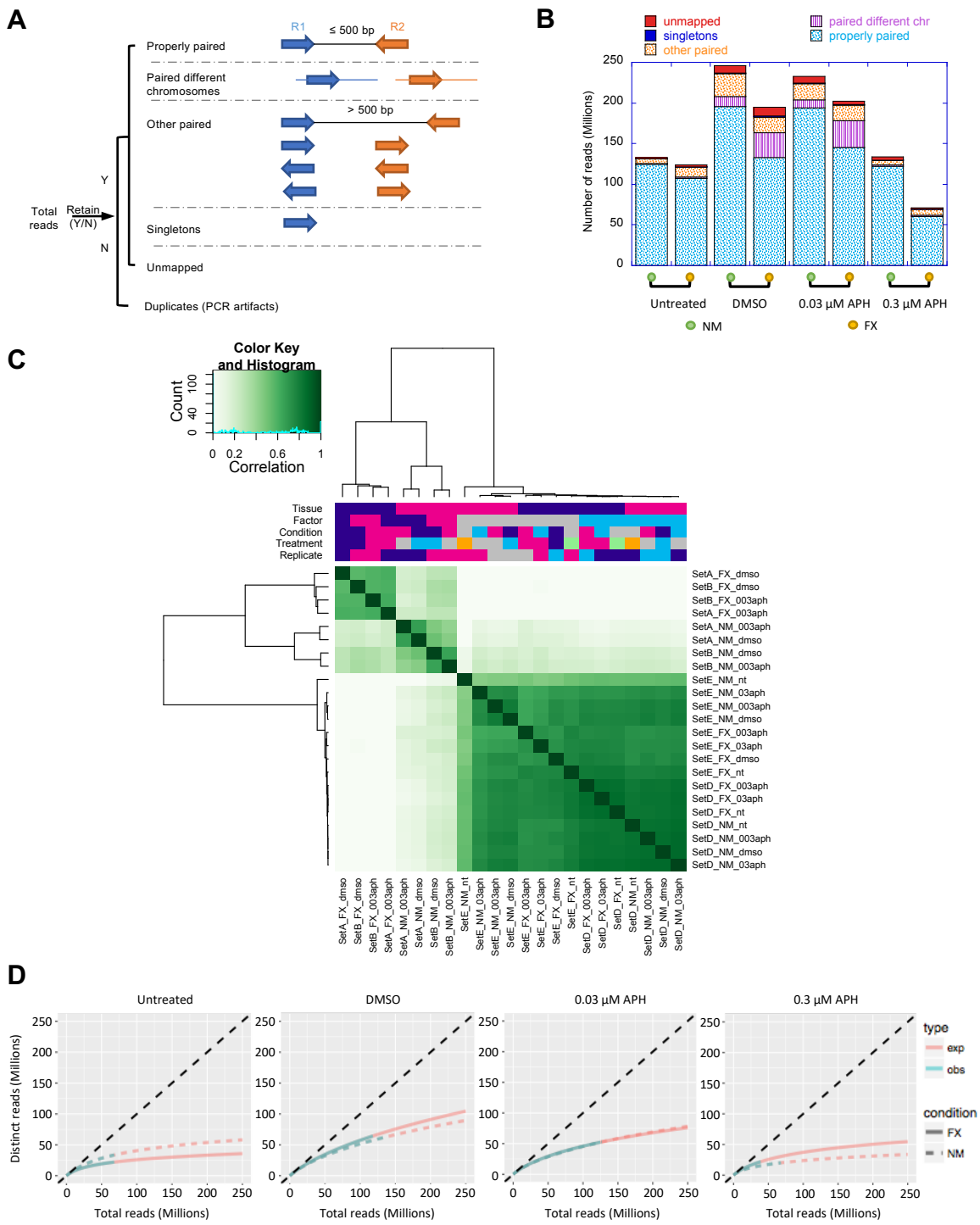


**Figure S4. Related to Figure 3. Break-seq data quality check.** (A&B) Break-seq library quality assessed by read classifications. “R1” and “R2”, Read 1 and Read 2, respectively. Samples with the same treatment were merged to assess overall sequencing depth in (B). (C) Break-seq experiments correlation heatmap generated by plot (FX.breakseq) in DiffBind. Note that FX\_dms0 has three instead of four replicates due to the removal of a dubious experiment (SetD\_FX\_dms0). (D) Break-seq library complexity of FX and NM cells (“obs” and “exp” stand for observed and expected library complexities, respectively). Libraries from biological replicates for each treatment condition were merged for complexity measure.

## Supplemental Figure S5

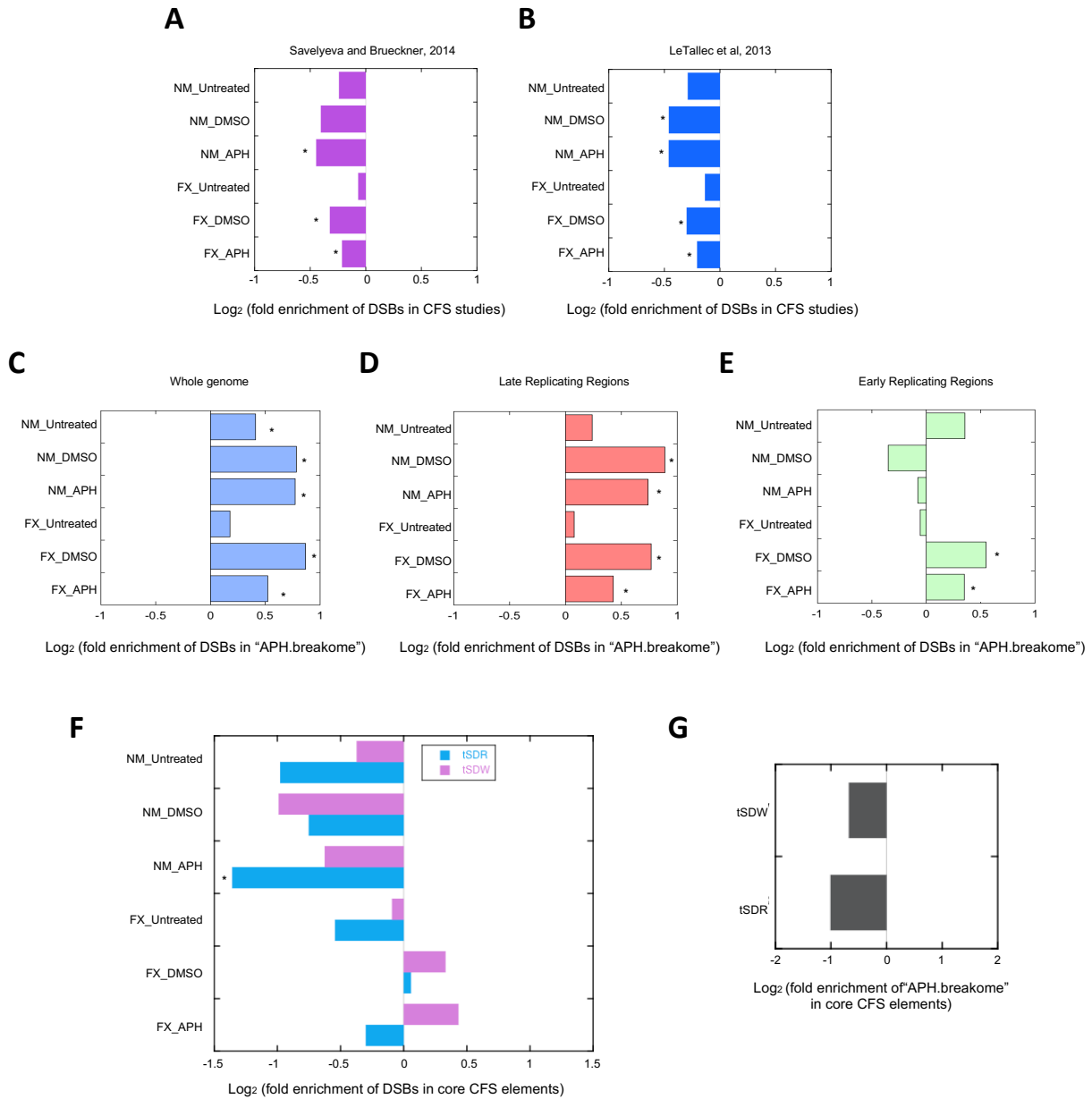
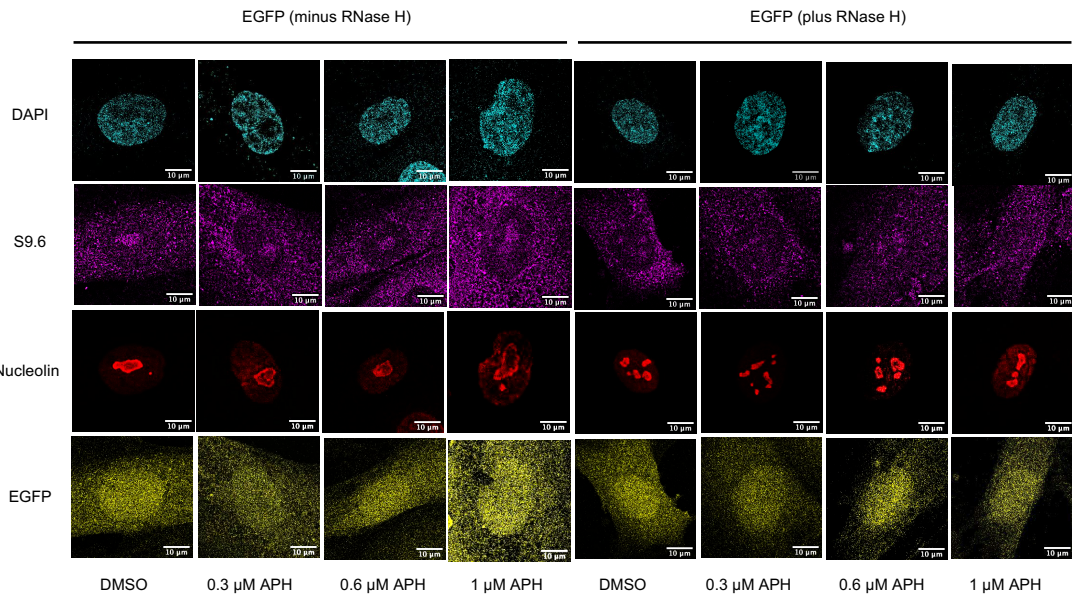


**Figure S5. Related to Figure 4D. Genomic Association Test (GAT) for correlations between DSBs in our study and CFSs reported in literature.** (A-B) Correlation between DSBs and reported CFSs. Log<sub>2</sub> transformation of the fold enrichment values (ratios of observed to expected number of DSBs) are reported for CFSs mapped by Salveleyeva and Brueckner, 2014 (A) and LeTallec et al, 2013 (B). Correlation between those DSBs that are concordant with the "APH.breakome" in the whole genome (C), the late replicating regions (D), and the early replicating regions (E). (F) Correlation between DSBs and the late-replicating CFS core elements containing large transcribed genes, defined as tSDWs (transcribed Significantly Delayed Windows) and tSDRs (transcribed Significantly Delayed Regions), in Brison et al. 2019. (G) Correlation between "APH.breakome" and the late-replicating CFS core elements containing large transcribed genes as in (F). Those samples marked with an asterisk indicate p values ≤ 0.001.

## Supplemental Figure S6

**A**



**B**

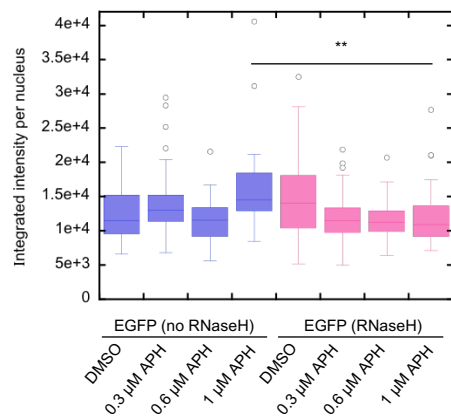


**Figure S6. Related to Figure 5. Nuclear RNA:DNA hybrid signals detected by S9.6 antibody is labile to RNase H treatment.** (A) Representative confocal images of immunofluorescence staining with S9.6 antibody in FX cells expression EGFP untreated or treated with RNaseH prior to staining. Scale bar, 10  $\mu$ m. (B) Quantification of nuclear S9.6 signals in three independent experiments ( $n \geq 36$  in each) using one-way ANOVA with multiple comparisons where \*\* $p < 0.01$ .

## Supplemental Figure S7

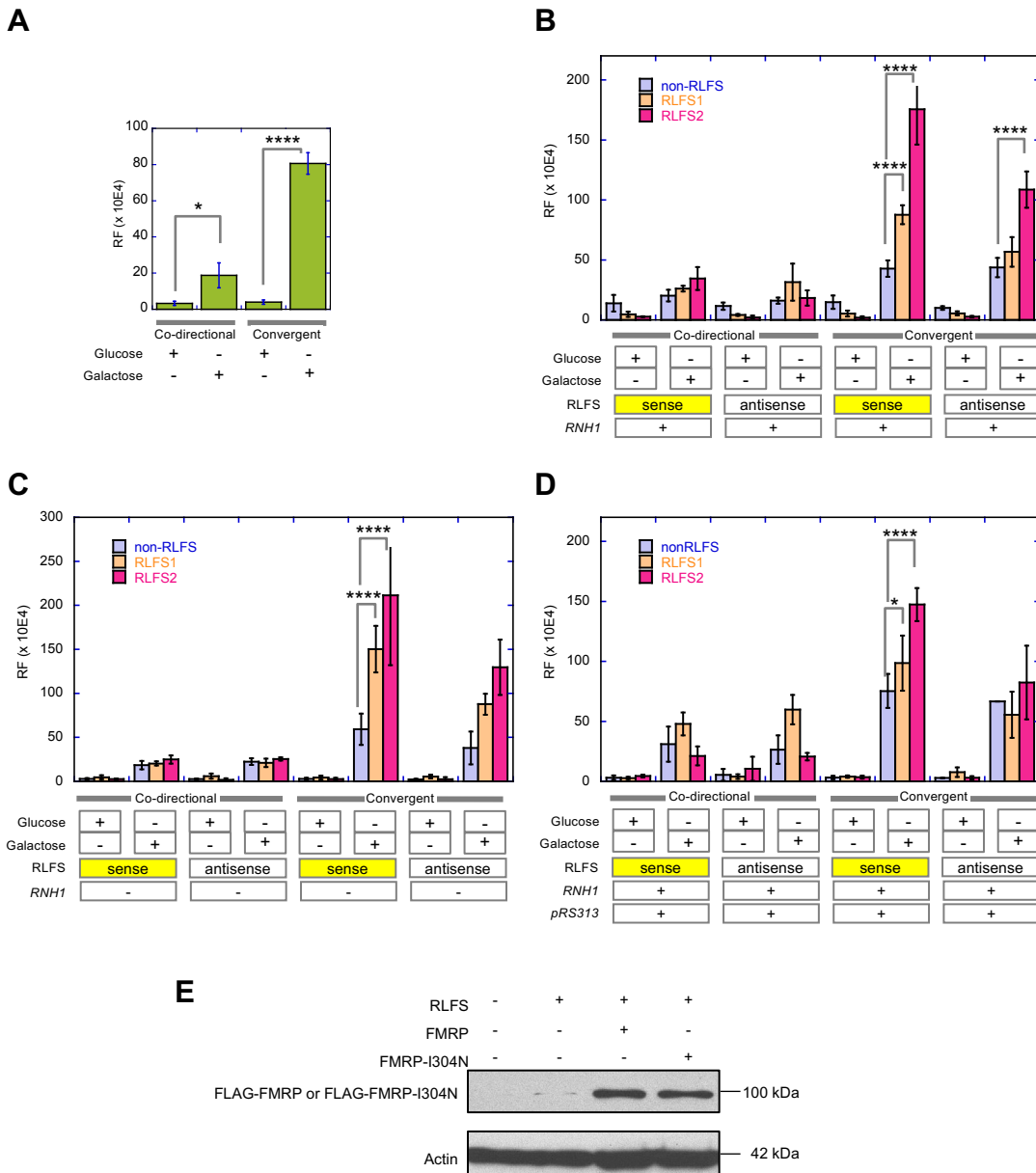


**Figure S7. Related to Figure 6. Control experiments for RLFS-induced DNA breakage and recombination frequency (RF) in yeast.** (A) RF is dependent on transcriptional activation. One-way ANOVA followed by Tukey's multiple testing was performed. (B) Insertions of RLFS elements from the human genome can further induce RF, specifically when inserted in the "sense" orientation with respect to transcription. (C) The RLFS-induced RF can be further enhanced by deletion of *rnh1*, the gene encoding for RNase H1. Note the change of scale on the Y-axis in (C). (D) Cells bearing a second plasmid, pRS313, which appeared to have little effect on RF, serve as control for the experiments in Fig. 3B. From (A) to (D) \*p<0.05 and \*\*\*\*p<0.0001. E) FMRP and FMRP-I304N show similar expression levels in yeast. Cells transformed with a plasmid with or without an RLFS in the LEU2 gene cassette, together with a plasmid with or without the CMV-driven and FLAG-tagged FMR1 or FMR1-I304N, were analyzed by Western blot using the anti-FLAG antibody. Actin served as a loading control.

## SUPPLEMENTAL TABLES

**Table S1. Related to figure 4C.** Number of consensus DSB peaks (detected in at least 2 replicates) in all categories defined by strain/treatment/comparison combinations.

DSB category <sup>1</sup>	Number of consensus DSBs
FX.APH	18473
FX.APH003	16796
FX.APH03	2112
FX.DMSO	9167
FX.NT	4149
FXdmso.FXaph.overlap	6177
FXdmso.FXaph.uniquetoFXaph	12296
FXdmso.FXaph.uniquetoFXdmso	2984
FXdmso.FXnt.overlap	322
FXdmso.FXnt.uniquetoFXdmso	8845
FXdmso.FXnt.uniquetoFXnt	3827
NM.APH	7002
NM.APH003	3506
NM.APH03	2161
NM.DMSO	3927
NM.NT	2111
NMdmso.NMaph.overlap	3209
NMdmso.NMaph.uniquetoNMaph	3792
NMdmso.NMaph.uniquetoNMdmso	714
NMdmso.NMnt.overlap	1651
NMdmso.NMnt.uniquetoNMdmso	2276
NMdmso.NMnt.uniquetoNMnt	458
FXdmso.NMdmso.overlap	644
FXdmso.NMdmso.uniquetoFXdmso	8523
FXdmso.NMdmso.uniquetoNMdmso	3283
FXnt.NMnt.overlap	1753
FXnt.NMnt.uniquetoFXnt	2396
FXnt.NMnt.uniquetoNMnt	358
FXaph.NMaph.overlap	4369
FXaph.NMaph.uniquetoFXaph	14104
FXaph.NMaph.uniquetoNMaph	2633

<sup>1</sup>Strain=FX, NM; Treatment=NT (untreated), DMSO, APH003 (0.03 µM APH), APH03 (0.3 µM APH), APH (composite of APH003 and APH03); Comparison=overlap (shared by two samples), uniquetoXXxx (unique to the sample indicated).

**Table S2. Related to figure 5G-H.** Select top Gene Ontology terms ( $p < 0.001$ ) for “Biological pathways” associated with DSBs in the indicated groups.

DSB Group	Biological pathway	P value	# of genes
FX_UNTREATED	neuron projection development	1.12E-05	100
	nervous system development	2.08E-05	214
	regulation of cell morphogenesis	2.08E-05	66
	synapse organization	5.29E-05	40
	regulation of neuron projection development	6.25E-05	58
	neuron development	8.09E-05	109
	neuron cell-cell adhesion	0.00015	9
	neuron projection morphogenesis	0.00018	70
	ion transmembrane transport	0.00025	107
	inorganic ion transmembrane transport	0.00048	85
FX_DMSO	cell projection organization	0.00030	187
	localization	0.00030	717
	cell part morphogenesis	0.00050	131
	inorganic ion transmembrane transport	0.00052	118
	neuron development	0.00075	146
	cell projection morphogenesis	0.00086	126
FX_APH	positive regulation of GTPase activity	6.76E-06	180
	regulation of cell morphogenesis	7.35E-06	139
	nervous system development	1.15E-05	504
	regulation of cell projection organization	4.09E-05	152
	neuron projection development	5.56E-05	213
	regulation of neuron projection development	9.09E-05	119
	cell adhesion	0.000107	405
	chemical synaptic transmission	0.000107	163
	movement of cell or subcellular component	0.000199	415
	cell projection assembly	0.000212	113
	vesicle-mediated transport	0.000347	343
	synaptic vesicle localization	0.000569	46
	microtubule-based process	0.000596	160
	synaptic vesicle cycle	0.000681	41
	dendrite development	0.000733	63
	cytoskeleton organization	0.000784	271
NM_UNTREATED	None		
NM_DMSO	None		
NM_APH	regulation of cell projection organization	2.20E-06	108
	regulation of cell morphogenesis	1.56E-05	94
	cell projection organization	3.97E-05	201
	regulation of neuron projection development	0.000217	80
	neuron projection development	0.000559	135
	neuron development	0.000559	154
	nervous system development	0.000646	305
	cellular component morphogenesis	0.000646	186
FX_DMSO_RLFS_overlap	flavonoid glucuronidation	0.000136	8
	cellular glucuronidation	0.000208	8
	uronic acid metabolic process	0.000499	8
	flavonoid metabolic process	0.000499	8
	flavonoid biosynthetic process	0.000499	7
	glucuronate metabolic process	0.000499	8
FX_APH_RLFS_overlap	single-organism membrane organization	0.001285	84

**Table S3. Related to figure 6A.** Correlation between DSBs in various groups and 169222 computationally predicted RLFSs (Wongsurawat et al., 2012) and 108011 composite DRIP-seq signals merged from all DRIP-seq data sets (NT2 and K562) (Sanz et al., 2016). Note the merged DRIP-seq dataset has 6.6 times the coverage of the RLFSs.

DSB group	Number of DSBs	Query (RLFS or DRIP-seq signals)	Number of DSBs overlapped with RLFS or DRIP-seq signals	P value Left	P value Right	P value Two-tail	Enrichment Ratio
FX.NT	4149	RLFS	133	2.34E-43	1	4.37E-43	0.358
FX.DMSO	9167	RLFS	1294	1	3.71E-37	6.24E-37	1.493
FX.APH	18473	RLFS	2323	1	1.25E-66	2.02E-66	1.498
NM.NT	2111	RLFS	129	7.31E-13	1	1.36E-12	0.552
NM.DMSO	3927	RLFS	659	1	1.22E-34	1.82E-34	1.746
NM.APH	7002	RLFS	554	0.045261	0.95877	0.089567	0.927
FX.NT	4149	DRIP-seq	526	7.62E-14	1	1.54E-13	0.717
FX.DMSO	9167	DRIP-seq	2658	1	1.07E-155	1.55E-	1.914
FX.APH	18473	DRIP-seq	4137	1	1.36E-80	2.21E-80	1.422
NM.NT	2111	DRIP-seq	389	0.64755	0.37359	0.73422	1.02
NM.DMSO	3927	DRIP-seq	1229	1	2.21E-90	2.98E-90	2.083
NM.APH	7002	DRIP-seq	1326	1	1.57E-06	2.93E-06	1.157

P values were calculated using bedtools Fisher's Exact Test. "NT", untreated.

**Table S4. Related to figure 6A.** Statistical analysis of absolute distance between RLFSS and DSBs in the indicated categories on each chromosome using GenometriCorr. Shown are the projection test p-values (P) and projection test observed to expected ratios (R). Samples with R values greater than 3.5 are shown in bold.

Chr	FX.Untreated		FX.DMSO		FX.APH		NM.Untreated		NM.DMSO		NM.APH	
	P	R	P	R	P	R	P	R	P	R	P	R
1	0.355	1.04	<b>2.22e-</b>	<b>3.79</b>	1.07e-	2.76	0.224	1.23	0.086	1.51	0.353	0.81
2	0.314	0.64	<b>2.21e-</b>	<b>3.62</b>	1.55e-	2.62	0.236	1.21	<b>1.73e-</b>	<b>3.79</b>	0.010	1.85
3	0.446	0.69	1.29e-	3.02	1.81e-	2.57	0.329	0.00	0.024	2.28	0.131	1.43
4	0.283	0.39	2.39e-	3.00	1.44e-	3.22	0.355	0.80	0.036	2.20	0.199	1.28
5	0.217	0.34	1.09e-	3.24	1.63e-	2.79	0.244	0.00	0.007	2.55	0.148	1.38
6	0.090	0.00	<b>6.36e-</b>	<b>3.74</b>	5.08e-	2.06	0.336	0.00	0.134	1.53	0.028	0.00
7	0.489	0.86	6.30e-	2.51	4.01e-	2.57	0.108	0.00	0.104	1.48	0.126	1.33
8	0.150	0.29	4.34e-	2.96	1.06e-	2.08	0.182	1.36	0.203	1.29	0.131	0.40
9	0.301	0.41	3.91e-	3.21	4.19e-	3.19	0.174	1.39	0.016	2.17	0.109	0.46
10	0.137	0.28	2.85e-	3.27	3.85e-	2.80	0.302	1.04	0.088	1.63	0.373	1.01
11	0.070	0.23	7.45e-	2.21	0.001	1.64	0.118	0.00	0.047	1.70	0.123	0.52
12	0.044	0.00	<b>4.91e-</b>	<b>4.04</b>	7.32e-	2.74	0.209	0.00	0.076	1.70	0.350	1.04
13	0.372	0.00	<b>9.55e-</b>	<b>6.96</b>	<b>8.71e-</b>	<b>5.43</b>	0.347	0.00	0.482	0.00	0.260	0.00
14	0.190	1.33	<b>8.41e-</b>	<b>3.51</b>	<b>6.05e-</b>	<b>3.81</b>	0.035	2.78	<b>5.87e-</b>	<b>4.21</b>	0.103	1.62
15	0.109	1.65	<b>3.62e-</b>	<b>4.23</b>	<b>2.64e-</b>	<b>3.92</b>	0.377	0.00	0.054	1.96	0.088	1.63
16	0.050	0.21	<b>0.00e-</b>	<b>5.66</b>	<b>0.00e-</b>	<b>4.52</b>	0.484	0.76	0.060	1.62	0.291	1.11
17	0.056	0.22	2.62e-	3.28	7.21e-	3.15	0.322	0.43	0.353	1.04	0.165	1.27
18	0.103	1.78	<b>1.14e-</b>	<b>3.96</b>	3.54e-	2.76	0.144	1.49	0.061	2.23	0.237	1.19
19	0.057	0.45	2.32e-	1.94	2.88e-	1.91	0.162	0.44	0.429	0.99	0.065	0.63
20	0.456	0.80	5.62e-	2.83	9.08e-	3.16	0.135	1.56	0.039	2.14	0.218	1.23
21	0.230	0.00	<b>5.01e-</b>	<b>7.10</b>	<b>2.22e-</b>	<b>6.00</b>	0.426	0.00	0.014	2.81	0.432	0.89
22	0.093	0.00	<b>1.80e-</b>	<b>5.34</b>	<b>3.99e-</b>	<b>3.76</b>	0.462	0.64	0.016	2.14	0.009	2.15
X	0.184	1.35	0.081	1.48	0.098	1.33	0.113	1.63	0.024	2.13	0.077	1.55
ALL	5.47e-	0.52	0	3.16	0	2.68	0.041	0.71	8.93e-	1.97	0.150	1.08

**Table S5. Related to figure 6A.** Number of genes containing DSBs in FX cells that overlap RLFSS or DRIP-seq signals.

DSB Group	Total DSBs	Genes containing	Genes containing	Genes containing
		DSBs*	DSBs that overlap RLFSS*	DSBs that overlap DRIP-seq signals*
FXdmso.FXaph.overlap	6177 (28.8%)	4121 (27.8%)	894 (33.1%)	2364 (37.8%)
FXdmso.FXaph.uniquetoFXaph	12296 (57.3%)	8715 (58.8%)	1427 (52.9%)	3113 (49.8%)
FXdmso.FXaph.uniquetoFXdmso	2984 (13.9%)	1990 (13.4%)	378 (14.0%)	778 (12.4%)
FXdmso.FXaph.total	21457 (100%)	14826 (100%)	2699 (100%)	6255 (100%)
<hr/>				
NMdmso.NMaph.overlap	3209 (41.6%)	2484 (41.4%)	523 (50.7%)	1240 (41.3%)
NMdmso.NMaph.uniquetoNMaph	3792 (49.2%)	2524 (42.1%)	153 (14.8%)	718 (23.9%)
NMdmso.NMaph.uniquetoNMdmso	714 ( 9.3%)	990 (16.5%)	356 (34.5%)	1042 (34.7%)
NMdmso.NMaph.total	7715 (100%)	5998 (100%)	1032 (100%)	3000 (100%)

\* Percentages in parentheses indicate the percentage of DSBs or genes in each of the three categories (e.g., XX.XX.overlap, XX.XX.uniquetoXXaph, and XX.XX.uniquetoXXdmso) over the sum of the three categories

**Table S6. Related to Key resources table for oligonucleotides.** Oligonucleotides used in this study is listed below.

Name	Source
5'-CGAGGTTAACATGGT GAGCAAGGGCGAGGAG-3' (pcDNA3_RMEGFP_JL_FWD2)	This paper
5'-ATTCGTTAACCTTGACAGCTCGTCCATGCC -3' (pcDNA3_RMEGFP_JL_REV2)	This paper
5'-TAACGAATT CATGGACTACAAGGACGACGAT-3' (pFRT_RMFMRP_JL_FWD2)	This paper
5'-GGTAGAATTCTTAGGGTACTCCATT CACGAG-3' (pFRT_RMFMRP_JL_REV2)	This paper
5'-TCagatctTCAGGCTGCACATTCTTTC-3' (control-1_F)	This paper
5'-CTCggatccTGCTTCACTGCAGTTCC-3' (control-1_R)	This paper
5'-CTCagatctTGATAATTACAAGGTACACGTTATTGC-3' (control-2_F)	This paper
5'-CTCggatccTTGGTTAGGATAATAAGCACTATGG-3' (control-2_R)	This paper
5'-CTCagatctGTAGACGCCTCACCTCTGC-3' (RLFS-1_F)	This paper
5'-CTCggatccTGC GG GTG TAA AAC ACTG AAA-3' (RLFS-1_R)	This paper
5'-CTCagatctCATAACTAAGCACTGTATGCC-3' (RLFS-2_F)	This paper
5'-CTCggatccCCTAGGGACAAGGGGAGGTA-3' (RLFS-2_R)	This paper
5'-CTGTGTACATGAGCAAAGACAAAGATATC-3' (SHE2-Y-F)	This paper
5'-CTGGAATTCTCAGTTTCAATT TACC -3' (SHE2-Y-R)	This paper
5'-CTGGGAATCCCCTAATTATGGCAAGGCAAG-3' (RNH1-Y-F)	This paper
5'-CTGGCGGCCGCACAGCATTATCGTCTAGATG-3' (RNH1-Y-R)	This paper